Design of a Compact, Workflow-Oriented Robot for Transbronchial Lung Biopsy

By

Stephanie Rae Amack

Thesis

Submitted to the Faculty of the

Graduate School of Vanderbilt University

in partial fulfillment of the requirements

for the degree of

MASTER OF SCIENCE

in

Mechanical Engineering

May 10, 2019

Nashville, Tennessee

Approved:

Robert J. Webster III, Ph.D.

Thomas J. Withrow, Ph.D.

Eric Barth, Ph.D.

Jason Mitchell, Ph.D.

To my loving parents, your belief in me is without measure.

ACKNOWLEDGMENTS

This work would not have been possible without many teaching mentors, friends, and family that supported and guided me along the way.

First and foremost, I want to thank Dr. Webster for his tremendous support over the last two years. Dr. Webster provided me mentorship that awakened in me new purpose with my work as I transitioned from my role as a collegiate soccer player. He continued to pay close attention to my development along every step of the journey, and I am indebted to his ability to ignite excellence in his students, even when they are unsure of their own potential at times.

I want to thank my committee, Dr. Eric Barth, and Dr. Tom Withrow, Dr. Bob Webster, and Dr. Jason Mitchell for their close attention and feedback on my thesis, and for their positive support along the way. Dr. Withrow, thank you for your unwavering positivity that graces the 5th floor of Olin. Dr. Mitchell, without your mentorship and collaboration this work would certainly not exist. I have learned immensely from you as a mechanical design engineer, and it has been an absolute pleasure to work closely with you (even the days that involved dissecting pig lungs).

Thank you to our collaborators at North Carolina: Dr. Ron Alterovitz, Alan Kuntz, Mengyu Fu, and Janine Hoelscher, and to Dr. Fabien Maldonado of Vanderbilt University Medical Center for his clinical expertise that was crucial to the success of this work.

To the best lab mates in the world, thank you all for your collaboration and friendships that made working in the Med Lab such a joyful endeavor. It would take a few too many pages to adequately thank everyone who had an influence in my time at Vanderbilt. To James Ferguson, Maxwell Emerson, Tayfun Ertop, Andria Remirez, Trevor Bruns, Patrick Anderson, Margaret Rox, Katy Riojas, Dominick Ropella, Patrick Wellborn, Michael Siebold, and Josh Gafford, thank you for your collaboration and time spent in helping me along the way. Trevor, I am indebted to your electronics troubleshooting

prowess and willingness to lend support at any time. To Max, Tayfun, and Margaret, thank you for your collaboration in conducting experiments and for each of your selflessness and friendship throughout the work of this project. To fellow soccer players Katy and Patrick Anderson, thank you each for your collaboration and being a constant source of positivity and laughter in the lab. Andria you are a natural leader in lab, and I thank you for your friendly guidance. James it has been a pleasure being your adjacent desk mate and Dom, thank you for your collaboration and for being a wonderful running coach for my first marathon.

Last but not least, thank you to my friends and family that have supported me long before my time at Vanderbilt began. To my dear friends Sydney and Shelby Payne, I am forever grateful of the friendship that has blossomed from our time as teammates at Stanford, and has grown into a fellowship around serving Christ. To my family, there are no words to encompass how your love has enabled me to carry my studies through to fruition. Especially to my mom Dana and twin sister Kenzie, I couldn't have done it without your support and friendship from afar. Thank you for believing in me.

TABLE OF CONTENTS

LIST OF TABLES

Table Page

LIST OF FIGURES

Chapter 1

Introduction

1.1 Motivation

Lung cancer is the leading cause of cancer-related deaths in the U.S., claiming 154,050 lives every year [1]. The five year survival rate for lung cancer is only 18% [1], partially because many patients have advanced-stage lung cancer at initial diagnosis. The findings of the National Lung Screening Trial [2] indicate a reduction in lung-cancer-specific mortality with CT scanning in at-risk people. As such, more effective screening has become the emphasis in the medical community for early stage detection of lung cancer. With increased screening, there also exists a clear need to correctly identify which suspicious nodules in imaging are harmful cancers that require treatment [3]. Acquiring tissue samples of the suspicious nodule through biopsy is essential to obtain a definitive diagnosis of cancer.

One approach to reach peripheral nodules of the lung is through percutaneous, or transthoracic, approaches. The percutaneous approach of biopsy requires inserting a needle from the outside of the body through the pleural lining of the lung to gather tissue samples for further histopathological analysis. This approach can have high diagnostic yield (74%) for larger nodules, but diagnostic accuracy for malignancy in nodules smaller than 10 mm in diameter falls off due to the technical difficulties of navigating to such a small lesion [4]. For nodules less than 1.5 cm in diameter, diagnostic yield is less than 52% [5]. Percutaneous access also

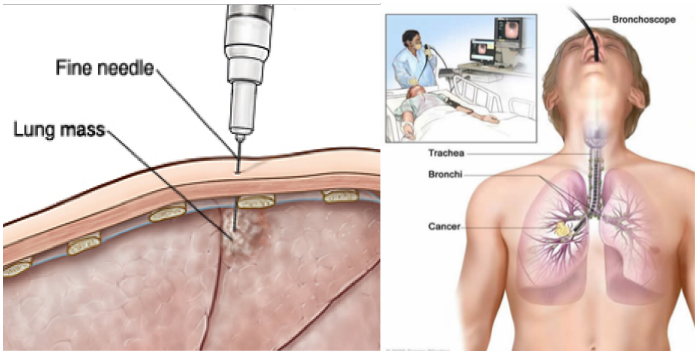

Figure 1.1: Left: Percutaneous Biopsy. Right: Transoral Bronchoscopy

carries a substantial risk of intraoperative complications including pneumothorax, or lung collapse, which occurs in as many as 28% of patients [6, 7]. In this approach, 5% of patients require interventional treatment of chest tube insertion [8] with other complications including parenchymal hemorrhage (8.5%) [6], hemoptysis (7%) [9] and occasional reports of embolism [10] and even death [11].

The other main approach to biopsy is through bronchoscopy. Physicians have transoral access to the lung through flexible bronchoscopes, which have tendon-actuated tips that enable manual steering through the airway. Physicians use their knowledge of anatomy and the scope's camera to navigate through the airway to a suspicious nodule for biopsy. Biopsy modalities including flexible aspiration needles, brushes, or biopsy forceps, are passed through the bronchoscope and used to collect several (4-6) [12] samples of the lesion [13].

Flexible bronchoscopy is effective in diagnosing nodules visible to its camera, and diagnostic yield has increased over time (75% in 2001 to 94.5% in 2007) [14]. However, bronchoscopy is limited since it cannot reach into the many airways smaller than the bronchoscope's diameter. [15]. Bronchoscopes vary in size, with outer diameters from 1.8 mm (ultrathin) to 6.9 mm (EBUS flexible bronchoscope) and working channels vary from 0.6 mm to 3.2 mm [16]. The diagnostic yield of bronchoscopy declines when the nodule is located far from the entrance of the lung, with yields of central, intermediate, and peripherally located nodules at 82, 61, and 53%, respectively [15]. While ultrathin scopes have increased the reach of flexible bronchoscopy from the 5^{th} to 11^{th} bronchus [16], the locations attempted using this technique are still within the airways, or in close proximity to them. Thus, there exists a clear need to leverage the safety of bronchoscopy, yet provide access to peripheral targets that are not located in or immediately adjacent to large airways.

1.2 Guided Bronchoscopy Techniques

In traditional bronchoscopy, it can be challenging for the physician to navigate to the location of a pulmonary nodules [17]. Recent technical advances in endoscopic imaging augment bronchoscopist's ability to visualize and navigate airways. Methods that augment traditional bronchoscopy with additional imaging or navigation assistance are called guided bronchoscopy. These include electromagnetic navigation bronchoscopy (ENB), radial endobronchial ultrasound (R-EBUS), and virtual bronchoscopy (VB).

Electromagnetic navigation bronchoscopy involves registering preoperative CT imaging to an electromagnetic sensing system to reconstruct the bronchoscope's position with respect to a visual representation of the lung displayed on a computer screen. Commercially available systems include SPiNDrive of Veran Medical Technologies [18] and SuperDimension from Medtronic [19] provide ENB navigation, with initial reports of overall diagnostic yield of 67% using the SuperDimension system [20].

Radial endobronchial ultrasound is widely used for lesions in close proximity to the bronchus. Endobronchial ultrasonographic biopsy is performed with a bronchoscope equipped with a linear array transducer that enables real-time ultrasonic guidance of a biopsy needle. A randomized trial comparing conventional (non-guided) biopsy to ultrasound guided (R-EBUS) biopsy revealed an increased diagnostic yield from 31% to 75% in lesions $\leq$ 3 cm [21] using the Endobronchial Ultrasound (EBUS) bronchoscope from Olympus [22].

Virtual Bronchoscopy features software that reconstructs CT data into 3D models of bronchial airways, vascular structures, ribs, and lungs to mark and segment a target. Virtual bronchoscopy differs from ENB in that it does not rely on real time positional signaling from sensors around the patient. The commercially available VB platform is the Archimedes Navigation system from Broncus Medical [23]. The Archimedes system also integrates a dilation balloon and tunneling sheath, attempting to provide parenchymal access to targets. However, this system is constrained in its inability to steer upon entrance into the parenchyma, limited to straight-line targets.

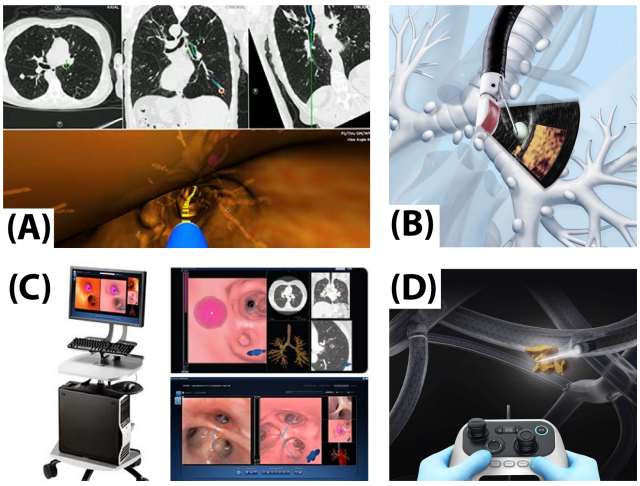

Figure 1.2: Commercial approaches to peripheral lung biopsy: (a) electromagnetic navigation (SPiNDrive, Veran Medical), (b) endobronchial ultrasound (EBUS Bronchoscope, Olympus), (c) virtual bronchoscopy (Archimedes, Broncus Medical), (d) robotic bronchoscopy (Monarch, Auris Inc.)

In a meta analysis, guided bronchoscopy reports a 70% diagnostic yield. While this is higher than traditional bronchoscopy (63%), it is as low as 14-34% for nodules under 2 cm [8]. So while guided bronchoscopy techniques increase bronchoscopist's ability to navigate accurately, there still exists an inability to accurately reach small, peripheral nodules, and controllably steer outside the airways.

1.2.1 Robotic Bronchoscopy

More recently, flexible bronchoscopy robots have been released (the Monarch system from Auris, Inc.) or are currently under development (the Ion system from Intuitive Surgical, Inc.) with the goal of improving yield in trans-bronchial peripheral lesion biopsies through enhanced distal dexterity. These systems combine the advantages of guided bronchoscopy with the mechanical stability and ease of use of a robot. While these platforms offer greater control of biopsy needles within the bronchus, these systems remain limited to the airways and immediately adjacent lesions, since they provide no way to steer through the parenchyma of the lung.

There has been large developments in visualization through ENB, R-EBUS, and VB options of guided bronchoscopy, but commercial efforts presented thus far are focused primarily on imaging and navigation. While robotics has entered flexible bronchoscopy, introducing distal dexterity of biopsy instruments in the airway, its reach is still limited to targets embedded in, or in close proximity to, those airways. To date, there is not a solution that augments bronchoscopy by introducing steering capabilities in the parenchyma.

1.3 A Robotic Platform for TransBronchial Lung Biopsy

Recognizing the merits and drawbacks of percutaneous and bronchoscopic approaches, our group has previously proposed combining steerable needles with concentric tube robots to enable peripheral lesion access and biopsy through bronchoscopic delivery platforms [24, 25, 26]. The workflow of this approach is displayed in Figure 1.3 and begins with manual operation of a flexible bronchoscope, augmented with our robotic platform to provide access from the airway to the parenchymal space of the lung. Our system introduces the ability to steer to peripheral nodules, acting as an extended working channel of the bronchoscope.

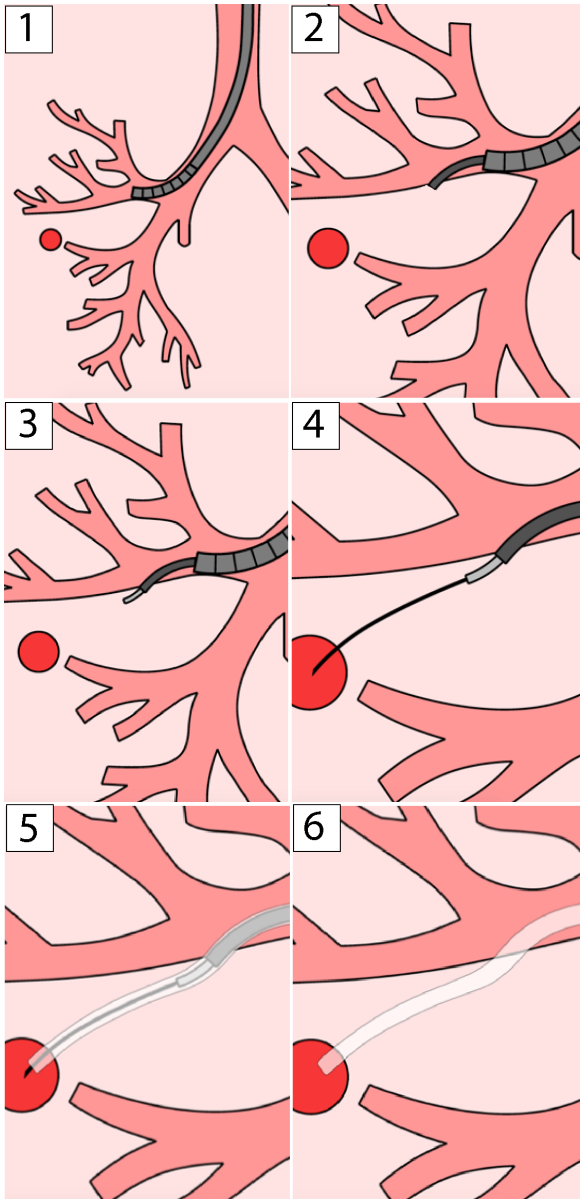

Figure 1.3: Envisioned robotic workflow: (1) the bronchoscope is manually deployed by the physician to target exit location in the bronchus (2) an outer concentric tube stage orients towards the bronchial wall for entrance into the parenchyma (3) a second concentric tube stage orients the needle (4) the innermost steerable needle stage is deployed to a target nodule (5) a sheath is slid over the steerable needle, and (6) the robotic assembly is removed leaving an extended working channel to the peripheral target

The workflow in this approach is as follows: (1) The physician first navigates a standard bronchoscope through the airway to the desired bronchial exit location, which may be manually selected by the physician or indicated using planning software developed with our

system [26]. After this, several robotically-controlled, nested tube stages are then deployed through the bronchoscope, as described in following steps. (2) A curved nitinol tube is used to reach from the bronchoscope tip to the planned exit location on the bronchus wall, where puncture into the parenchyma is performed. (3) Once in the parenchyma, a second concentric tube aims a steerable needle stage so that the desired target lies within its workspace. (4) The steerable needle leverages tissue interaction forces through a beveled, flexure hinge tip, achieving high curvatures with reduced tissue damage [27]. The needle is steered to the target under image guidance, with feedback from an electromagnetic sensor embedded in the tip of the needle. A sliding-mode controller [28] is used to guide the needle along a planned path avoiding critical structures in the lung to the peripheral lesion [26]. (5) Finally, a standard clinical sheath is passed over the entire nested tube assembly within the bronchoscope port to the target. (6) Upon successful targeting of the lesion, the nested tube assembly and the robotic unit are then removed, leaving the plastic tube in place. The end result is an extended working channel for the bronchoscope, through which standard biopsy instruments or therapy (e.g. laser ablation or chemotherapy) can be delivered to the desired target.

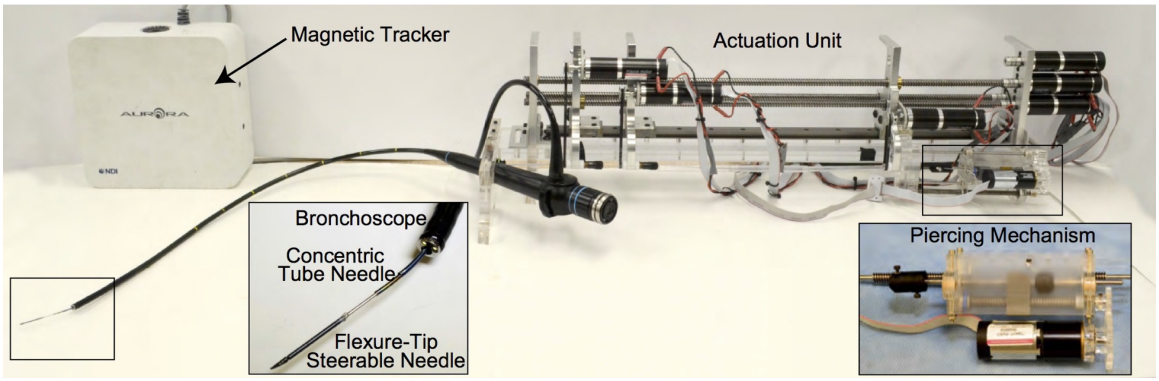

Figure 1.4: Actuation unit used in the proof-of-concept robotic system

This multi-stage, robotic approach aims to combine the high diagnostic yield of percutaneous biopsy with the reduced invasiveness and morbidity of transbronchial approaches. The primary focus of past work was on demonstrating feasibility of the multi-stage deploy-

ment concept, leaving opportunity to develop the robotic unit, workflow, and end effector tool designs to future work. An original actuation unit was constructed to test system feasibility, shown in Figure 1.4, but the design goals and constraints specific to peripheral lung biopsy had yet to be explored with the design. Workflow integration of the robotic unit to existing flexible bronchoscopy platforms is key to advancing the system towards clinical use, as is tuning the design of the concentric tube and steerable needle stages to achieve increased steerability in tissue.

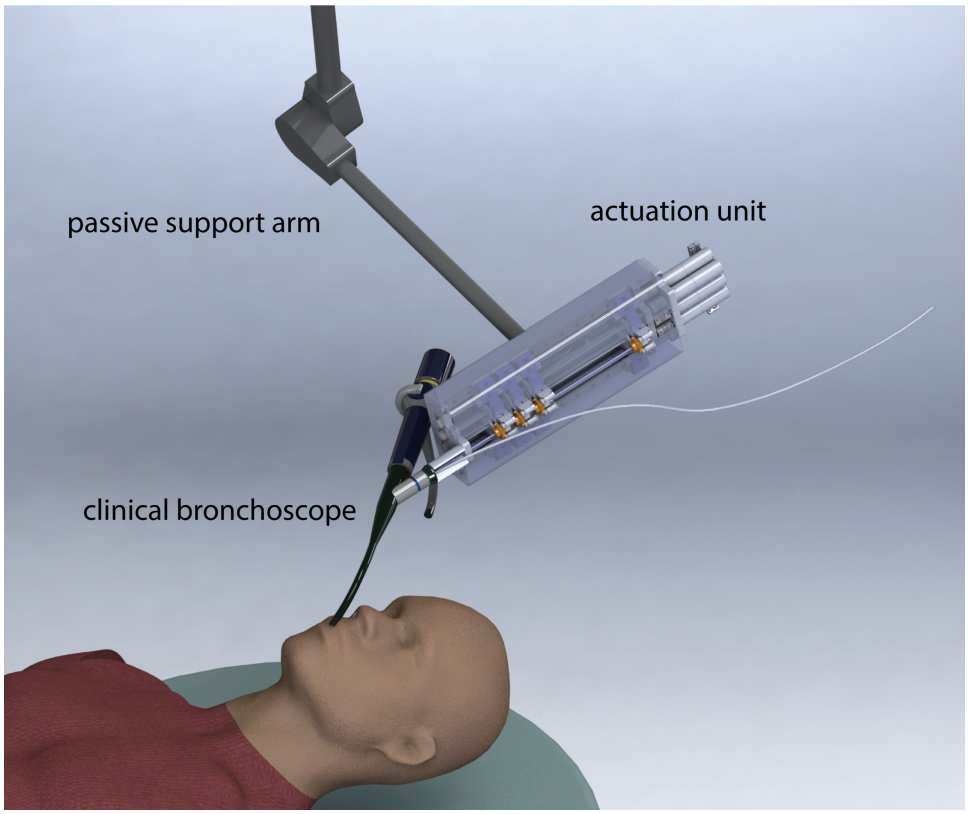

Figure 1.5: Rendering of the envisioned robot and bronchoscope: the concentric tubes, steerable needle, and sheath (referred to collectively as a "tool" throughout this thesis) are loaded into the bronchoscope and coupled to the actuation unit, which is held on a passive support arm and coupled to the bronchoscope after the physician deploys the bronchoscope. A standard clinical sheath is loaded with the tools of the actuation unit, and is progressed over the entire nested tube assembly within the bronchoscope port to the target.

1.3.1 Thesis Scope

This thesis contributes a novel electromechanical design that fits seamlessly within the existing clinical workflow of performing lung biopsy. Through compact design and ease of tool loading, the advancements in this thesis pave the way to bringing the innovative combination of concentric tube robots and steerable needles first proposed by Swaney et al. [25, 24] closer to the operating room. We present a new robotic hardware system design, tailored towards smooth integration into current bronchoscopy practices. Improvements in tool design increase the effective workspace of steerable needles crucial to practical peripheral lung targeting.

Chapter 2 includes a discussion of the constraints and specifications in designing a robotic actuation unit for peripheral lung biopsy. Chapter 3 discusses recent developments in tool improvements for increased steerability in targeting. In Chapter 4, we present the new robotic actuation unit design with novel mechanical features and sensing systems. Chapter 5 discusses control and experimental validation of the system through accurate closed loop-targeting of the steerable needle stage. Finally, Chapter 6 provides an overview of future development of the system and summarizes the contributions of this work.

Chapter 2

System Specifications

2.1 Design Goals

Developing and integrating a robotic system into clinical practice requires careful consideration of the clinical workflow and the constraints imposed by the operating room environment. Introducing robotic manipulation into a dominantly manual workflow like bronchoscopy requires design tailored to its application. Toward integration into the operating room, the design of endoscopic robotic systems emphasize compactness [29, 30, 31, 32, 33, 34, 35], leveraging features such as being lightweight and coexistence with existing platforms for adoption into the clinical space [36, 37]. Another important aspect of making a practical robot of this type for the operating room is developing a specific technique for homing, the process of returning the tubes to a known location ("home position") on the robot. We envisioned a modular system with a diverse toolset that could be efficiently coupled and decoupled from the system with ease, and that integrated positional sensing. With concurrent development of concentric tube and steerable needle designs, the ability to both interchange stages, and efficiently "home" the tool's pose in the research setting became a key design goal for the mechanical unit.

Another key requirement that is always important to consider in medical robotics is designing for safety and sterility. With a recent study of the reprocessing of flexible bronchoscopes calling for improved post-processing of bronchoscopes and heightened bronchoscopic sterility protocols [38, 39, 40], the design of this peripheral lung access system was aimed towards addressing future sterility protocols in which tools could be disposable. To this end, a design goal of this system was to introduce a means to couple tools to a transmission unit, that could potentially be bagged in a sterile field in the future.

In section 2.2 we inform the geometry of our compact transmission design by charac-

terizing the surgical workspace of our system. Section 2.3 outlines design decisions for the actuation of the system, creating a set of metrics used in the subsequent design of the compact mechanical actuation unit.

2.2 Anatomical Constraints

In order to determine the mechanical design specifications for the actuation unit, it was crucial to characterize the surgical workspace. To arrive at these design goals, we explored anatomical geometry to estimate the overall insertion distance required in the system. In this section, we inform our transmission design by analyzing how far each stage of our system needs to travel in order to supply sufficient workspace for targeting any desired point in the lung.

Referring back to the workflow of our system in Figure 1.3, the bronchoscope is initially roughly parallel to the airway, and deploys an outer concentric tube from the tip of the bronchoscope to reach the bronchial wall. The outer concentric tube acts as a delivery stage for the second concentric tube stage and flexure-tip needle, which enter the parenchyma. Thus, the required travel length of the outer tube depends on the position of the bronchoscope tip in the bronchus lumen, and the diameter of the bronchus.

The main bronchus is approximately 12 mm in diameter [41], and this diameter decreases each time the bronchus branches. To deploy the outer concentric tube from the port of a standard bronchoscope to the lining of a 12 mm diameter airway, we estimate the curved outer tube to require approximately 20 mm of insertion length based on an outer tube with a radius of curvature of 30 mm. Incorporating a factor of safety to account for variations in airway size between individual patients [42], we choose a maximum insertion length of 50 mm for the outer concentric tube.

The travel requirement for the second concentric tube stage was estimated in the same manner. We anticipate the insertion length of the second stage to be an even shorter distance- just enough to orient the steerable needle's workspace in the parenchyma. With a

highly curved stage, we estimate only 10 mm of insertion is necessary to orient the flexure-tip needle. With a safety factor, we design for 30 mm of travel length. This is a safe upper bound for this stage, as improvements discussed more in section 3.2 enable shorter insertion lengths of this stage due to a shorter curved section.

The travel length of the flexure-tip needle stage depends on lung anatomy and nodule locations in a given patient. To obtain an estimate for the maximum required needle travel length, we analyzed CT scans in 3D Slicer [43]. To perform this analysis, we consulted with an experienced bronchoscopist to select a number of points near the periphery of the lung as potential targets for our system to access. For each, we asked the bronchoscopist to identify the location he would use to exit the bronchial tree to reach that lesion location, for which he assumed the use of a standard, 6 mm outer-diameter bronchoscope to size the appropriate airway, shown in Figure 2.1. Anonymized CT scans of three male and two female lungs, at full inspiration, were analyzed to characterize the required distances.

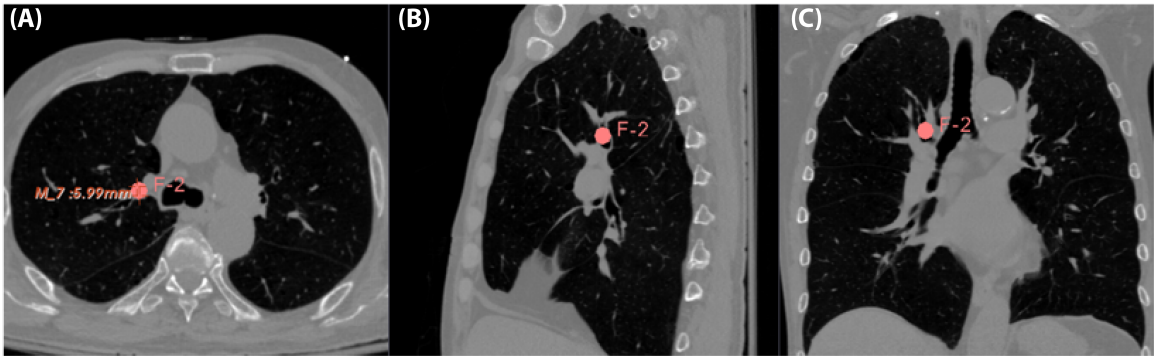

Figure 2.1: *(A)* axial *(B)* sagittal *(C)* coronal views of a 6 mm diameter bronchus exit location of our system

Each measurement took into consideration the boundaries of each lobe of the lung, since breaching pleural linings can lead to pneumothorax. The human lung consists of an upper, middle, and lower right lobe and an upper and lower left lobe. Peripheral targets were selected for each lobe for each patient scan, in the interest of identifying the largest linear distance reflecting a potential trajectory of our steerable needle.

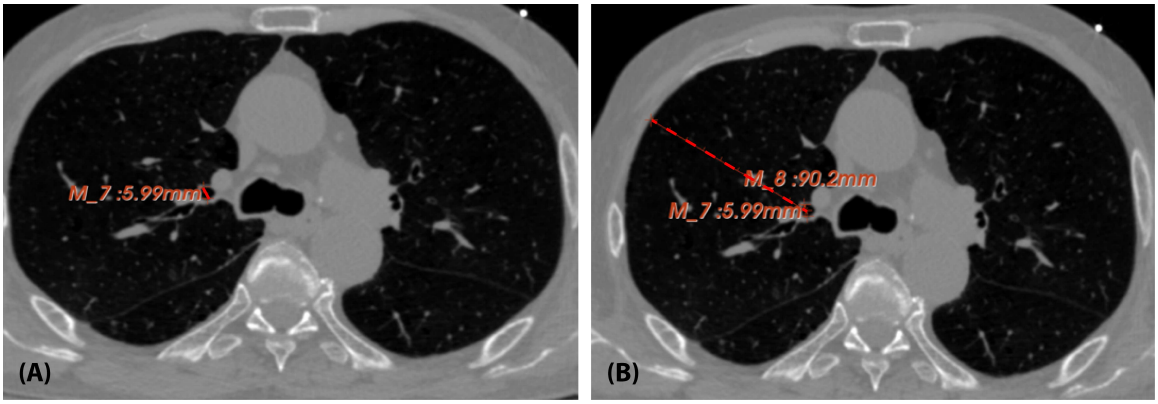

Figure 2.2: *(A)* Axial view of bronchus exit *(B)* Planar approximation of the needle travel to the lung periphery from the chosen bronchus exit

Using volume reconstruction of the lung to conduct the measurements enables 3D measurement of a potential path within a lung lobe. A planar example measurement is shown in Figure 2.2 (*B*). The straight-line approximation between each point of interest was confirmed to be within lobe linings, to ensure the path does not puncture the pleura, by viewing the line approximation in orthogonal views shown in Figure 2.3 (*B*).

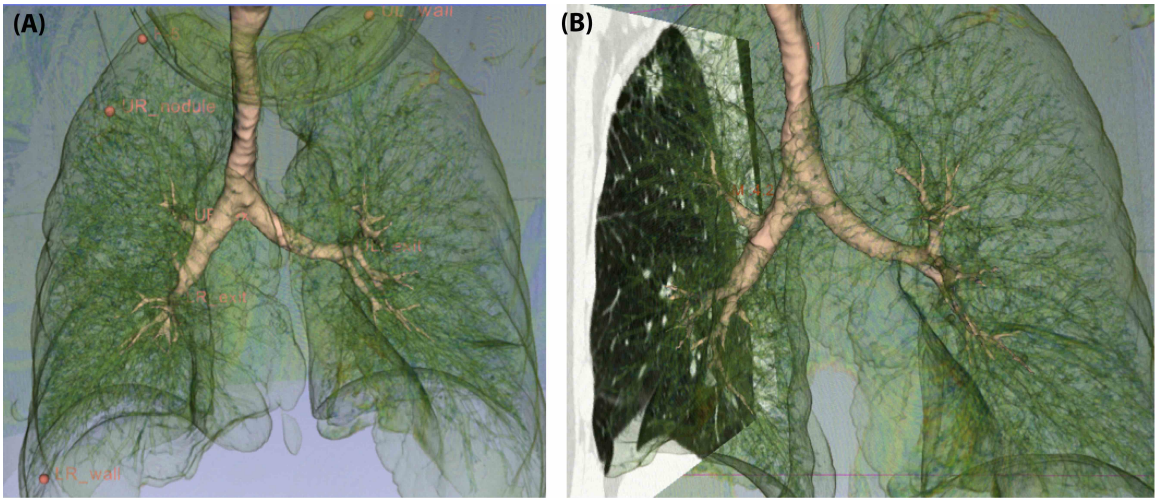

Figure 2.3: *(A)* Volume reconstruction of a lung with boundary targets approximated at the outer pleura *(B)* planar views were used to confirmed boundary targets lied between the fissures that separate the lobes of the lungs

An interesting finding arose from this case study of three males and two females. While we expected a larger male lung to correspond to longer measurements, we found that

smaller airways of female subjects limited the travel of the bronchoscope. As a result, the distance from the airway to the outermost part of the lung corresponded to similar measurements across male and female scans. While this is far from a comprehensive study on this subject, these initial findings suggest that the steerable needle stage will require similar insertion lengths for both male and female anatomies.

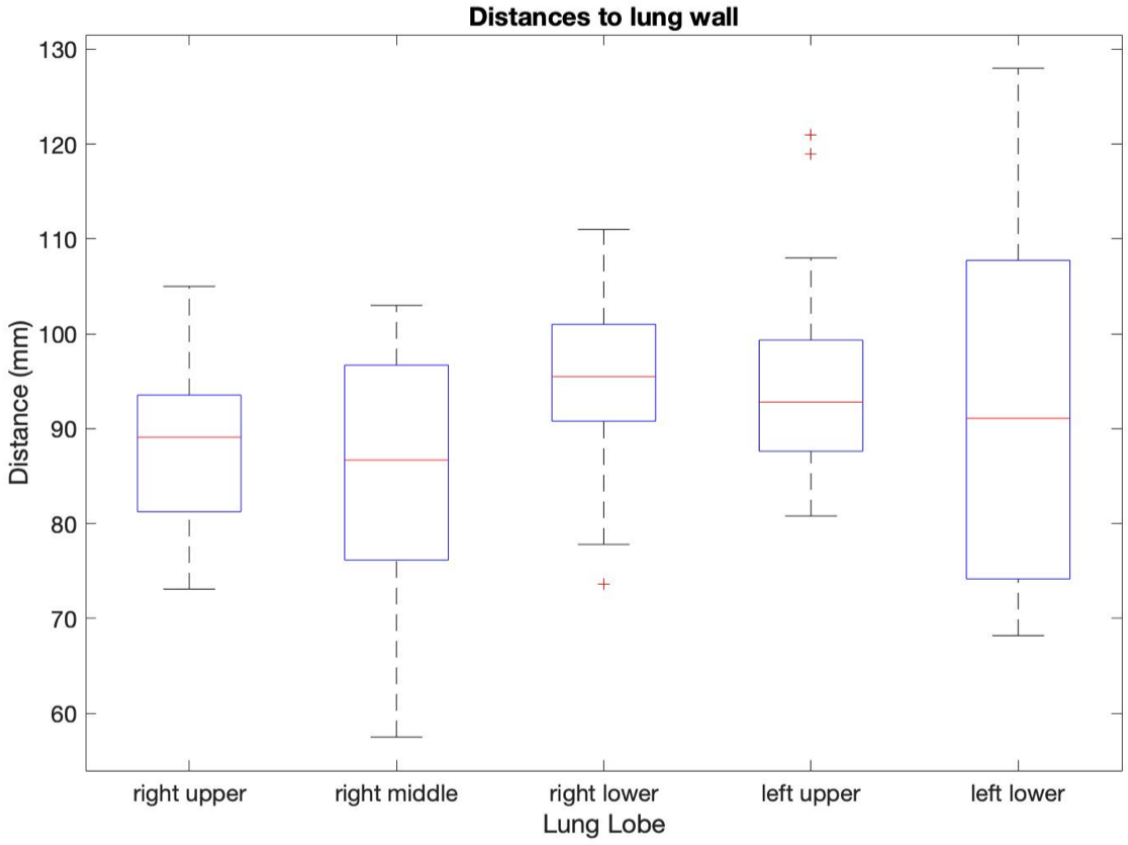

Figure 2.4: Measurements collected to estimate the travel requirements of the steerable needle in the lobes of the lung, with a maximum distance of 128 mm in the lower left lobe.

The graph in Figure 2.4 shows that the average distances in each lobe range from 85-95 mm, an overall mean between all lobes is 91 mm, and a maximum measurement of 128 mm was recorded in the left lower lobe. This provides us an estimate of how long to design for the linear travel of the needle across patient anatomies and varying geometries of lung lobes.

To account for potential variations in patient anatomy and the curvature of the steerable needle path within tissue, we design for more needle travel than simply the longest linear distance observed in our study. In prior steerable needle experiments, the radius of curvature of the flexure-tip needle was found to be approximately 250 mm [44], and correlates to a small addition of < 2 mm on the straight-line estimate. Based on these measurements and incorporating a safety factor, we design the length of this stage to accommodate 140 mm of travel to ensure that the lung system will be able to access all areas of the lung that may be of interest to biopsy. The total length of the actuation unit was designed to enable 220 mm of total travel, based off of the estimates we found for each stage.

2.3 Actuator Selection

Toward achieving compact design in the actuation unit, we used brushless DC motors capable of high power and speed transmission, densely packaged into diameters of less than 2 cm. We design the system's insertion and rotation speeds practical to parenchymal needle steering, which were estimated in prior benchtop experiments to be approximately 5 mm/s and 3.5 rad/s, respectively. We over-designed our actuators to ensure we do not reach their stall torques during use, selecting high power (8W), high-speed (EC-max 16) brushless DC motors (Maxon Precision Motors, Inc) with a nominal speed of 7350 rpm and torque of 8.19 mN-m. Gearheads were selected to achieve appropriate speeds and torque transmission for rotation and translation actuation. For translation actuation, we used a 29:1 gearhead to increase torque and reduce the nominal speed of the output of the shaft to 253 rpm at 237 mN-m. Driving a single-start lead screw of 1.27 mm pitch, our system achieves nominal 3.2 mm/s insertion speeds. Anticipating higher torque and lower speed requirements for the rotational motors to overcome loads due to torsional windup inherent in the system, we used a gearhead of 84:1 to provide output speeds of 87.5 rpm at 687.96 mN-m, resulting in a nominal angular velocity of 9.16 rad/s.

To validate the linear actuator selection, we measured the force to puncture ex-vivo

porcine tissue and compared it to the motor's nominal values. Using manual insertion, a beveled needle was attached to a hand-held force sensor to record peak forces to puncture out of the bronchus of ex-vivo porcine lung. This average force required to puncture the bronchus was 4.5 N, with a maximum of 5 N observed when using a large, 1.64 mm diameter needle. Repeating these tests using the actuation unit to perform automated insertion at speeds of 2 mm/s, 2.5 mm/s, and 3 mm/s, we found an average puncture force of 5.8 N. These latter tests were performed using the flexure-tip needle, held constrained by an outer tube to protect the flexure hinge. While using the flexure-tip needle to both puncture the bronchus and steer through the parenchyma is a more efficient workflow, we discovered that a sharp, stylet needle may be most appropriate to puncture the bronchial wall. Given puncture forces of $\leq$ 6 N, our linear actuator selection is appropriate in transmitting this force. The torque τ required to transmit force F using a leadscrew with lead L and efficiency η is:

$$\tau = \frac{F \cdot L}{2 \cdot \pi \cdot \eta} \tag{2.1}$$

Our lead screw features an estimated efficiency of 40%, a lead of 0.05", corresponding to a required torque of 3.03 mN-m to transmit the puncture force measured above, which is well below the nominal capabilities of our actuators.

In Chapter 2, we analyzed the clinical application to develop an initial set of functional requirements which were used to drive the design of the robot and its respective components. Linear travel requirements outlined in section 2.2 and actuator selection discussed in section 2.3 provide metrics for compact design of the mechanical unit. We add to this discussion in Chapter 3, detailing the design of the tool components of the system, which further influence the manipulation requirements of the robot.

Chapter 3

Tool Design

So far, we have begun to define the minimum required size for our compact design by defining the necessary linear travel of the various stages, and selecting of appropriate actuators for the system. We now elaborate on the design of the "tool", i.e., the concentric tubes and steerable needle themselves. Our design consists of a flexure-tip steerable needle, a wrist, a curved outer tube, and an outermost therapy delivery sheath nested in the bronchoscope as shown in Figure 3.1. In this section, we outline developments to the end effectors of our system, aiming to increase the tool's overall workspace. We begin with a look into the design of the innermost steerable needle stage, exploring ways to increase its curvature in a composite needle design.

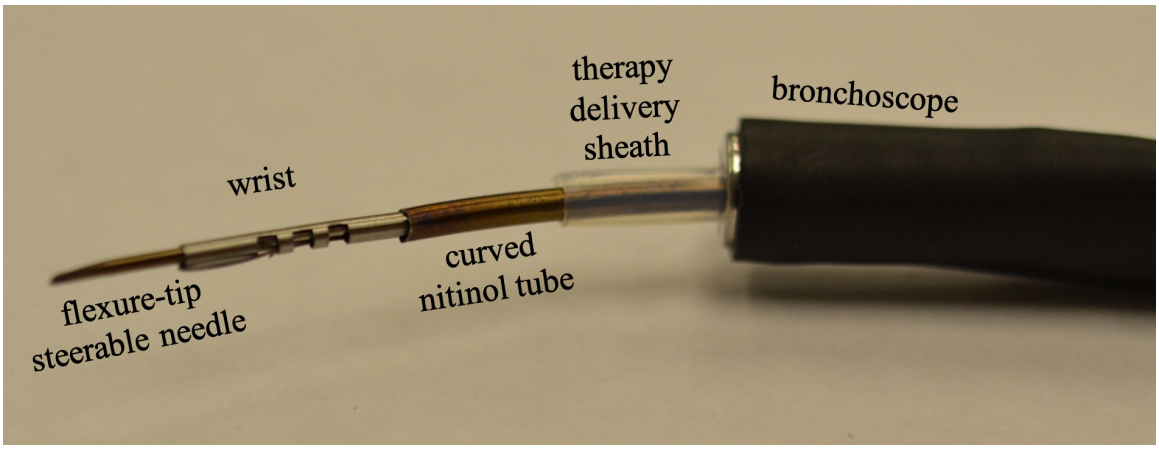

Figure 3.1: The complete tool assembly featuring a flexure-tip steerable needle, wrist, curved outer tube, and therapy delivery sheath. After manual deployment of the bronchoscope through the airway, the tools are loaded down the port of its working channel.

3.1 Flexure-Tip Needle Design

Needle insertion is a major part of minimally invasive procedures, enabling both diagnostic procedures through biopsy and therapeutic procedures such as ablation and drug

delivery. Robotic needle steering has shown promise to improve needle insertions, correct needle trajectory inside tissue, and may also enable new procedures currently not feasible with straight needles [45, 46]. Significant work has been done on needle steering design and is reviewed in [47], detailing methods to induce steering via passive or active manipulation. Steerable needles are aimed using the geometry of the needle's beveled surface [48, 49, 50, 51, 52, 53], kinked-tip designs [54, 55], flexibility in the needle shaft [55, 56] and more recently, through passive flexure hinge tips [27]. The passive flexure hinge tip in [27] demonstrated its ability to achieve curvatures similar to kinked-tip needles while reducing tissue damage and without requiring active, mechanical actuation of the hinge [57]. In this system, we leverage the passive flexure-tip needle steer in the lung, seeking to increase its curvature while integrating closed-loop, robotic control of the tip. In this section, we present developments to a new design of the flexure-tip needle and present how parameters of the design effect curvature in porcine loin tissue.

We design the flexure-tip steerable needle for increased curvature while integrating an electromagnetic sensor and maintaining robustness of the flexure hinge against forces in biological lung tissue. Shown in Figure 3.2, previous designs of the flexure-tip needle presented in [27] featured adhering the needle tip to its shaft using thin nitinol wires to generate bidirectional bending. While this design was effective in producing passive flexure motion, it limited our ability to load an electromagnetic sensor into the tip of the needle, since the lumen of the needle tip was utilized by the flexure hinge wires. The manufacturing process

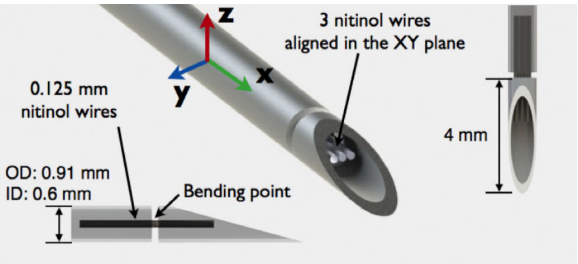

Figure 3.2: Previous flexure-tip designs featured hinges made from aligning nitinol strips of wire

was also time-intensive and consistency between needle designs proved difficult. To overcome this, we use computer numerical control (CNC) manufacturing, as described in the needle-sized wrist of [58] and later used to make flexure-tip needles in [44]. The flexure hinge is created by milling a slot into the wall of the nitinol tube tip, thereby introducing a preferentially weak point in the tube to create the flexure element, while leaving the lumen open for the magnetic tracking coil and its wires.

Throughout this system we seek to minimize the diameters and wall thickness of each stage to achieve flexible deployment through the bronchosocpe. Beginning at the steerable needle stage, we sought methods to scale down the needle. The size constraint of the system is integration of a 0.41 mm diameter sensor (Northern Digital, Inc.) into the steerable needle for closed-loop control. Selected for its small diameter and length, the 5-degree-of-freedom (5-DoF) sensor, with 4.9 mm length, is the most compact commercially available sensor to date compatible with the Aurora electromagnetic tracking system.

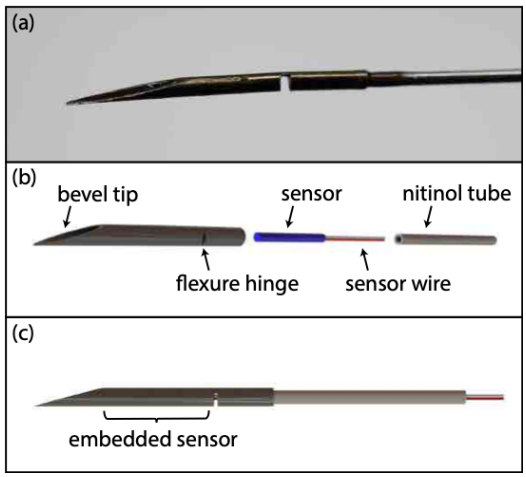

Figure 3.3: (a) Flexure-tip steerable needle prototype, (b) components of steerable needle, and (c) assembled needle with embedded electromagnetic sensor.

We chose the location of the flexure joint to be proximal to the bevel tip and sensor, to leverage a longer tip length of 8 mm. Previous work shows needle curvature is sensitive to tip length, and larger tip lengths enable increased curvature in kinked-tip needles [52, 59]. Prototypes using this design yield high curvature results and increase sensing accuracy of the needle tip position, since the larger needle tip enables the sensor to be loaded at the distal, beveled tip of the needle. We use a larger diameter needle tip to house the sensor and flexure hinge, while coupling to a tube of lower stiffness as the needle shaft to enable higher curvature.

To select the shaft of the needle, we look to reduce its stiffness while being able to transmit force through tissue. Stiffness is defined as the resistance of an elastic body to deflection, k, and is dependent on the elastic modulus, E, moment of inertia about the principle axis I, and the length in bending, L of the body. Given constant E and L values of superelastic nitinol needle shafts, we are interested in the effect of the diameter and the wall thickness on the moment of inertia on the stiffness of the shaft, which increases to the fourth power with diameter (outer diameter d_o, inner diameter d_i).

$$k = \frac{3EI}{L^3} \quad \text{where} \quad I = \frac{\pi(d_o^4 - d_i^4)}{64} \tag{3.1}$$

We found a 0.5715 mm nitinol tube of 0.127 mm wall thickness, and resulting moment of inertia of 0.0047 mm^4 provided good steering in deflated porcine lung. The resulting needle had a tip of 0.80 mm OD, 0.62 mm ID, and shaft of 0.57 mm OD, 0.32 mm ID, and was used in subsequent testing.

Using the slot-machined flexure-tip needle design, there are a number parameters that can be altered to affect the performance of the needle tip: location of the flexure joint, bevel angle, cut depth, and cut width. These parameters are highly dependent on one another, and can be tuned for performance in specific tissue. To that end, we sought to test the performance of our needle in various stiffness tissues. We used tissue samples of porcine loin, synthetic Ballistic gel (Humimic Medical, Fort Smith, AR) #3, and Ballistic gel #5, listed in decreasing stiffness. Testing in fresh porcine loin enabled us to compare curvatures of the new slotted flexure-tip needle design to past performance of the wire-hinge flexure-tip conducted in porcine loin, while the other tissue samples of decreased stiffness better predict the needle's performance in less dense, inflated lung. The reason for using these homogeneous tissues instead of lung tissue for initial needle design comparison, is due to poor navigation and visualization ability. Without implementing path planning and avoidance of distal bronchial airways, porcine lung proved a difficult medium to produce comparable needle design experimental results. A more complete optimization and kine-

matic characterization of needle performance in lung tissue will follow these comparative tests.

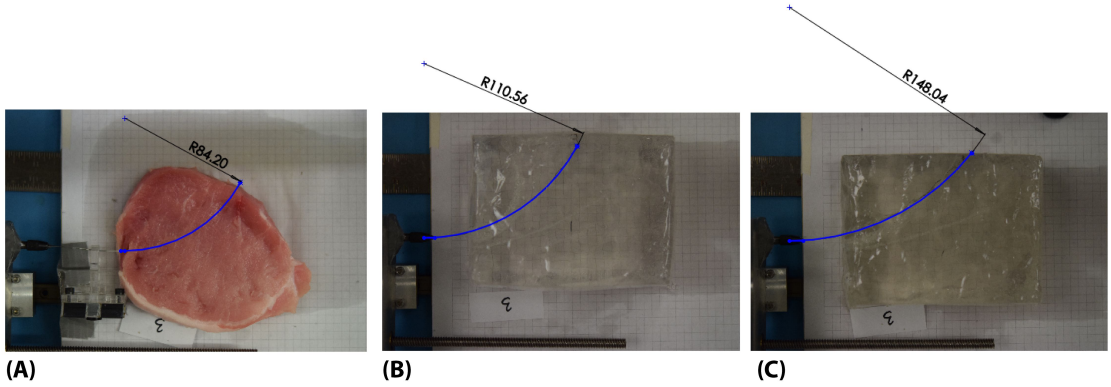

Figure 3.4: The flexure-tip needle described achieved a radius of curvature (ρ): (A) 84.2 mm in porcine loin, (B) 110.56 mm in Ballistic gel #3, (C) 148.04 mm Ballistic gel #5.

Through iterative prototyping and testing, we identified the following combination of parameters shown in Table 3.1 to produce a radius of curvature of 84 mm in porcine loin shown in Figure 3.4 (A), which is an improvement of the previous needle designs, recording an increase of curvature from 176 mm previous tests [44]. We saw an increase in radius of curvature in the less dense gels, with 148 mm in gel #5. These results show the current needle parameters achieve appreciable curvature and show promise in less dense tissues. Further fine-tuning of the flexure hinge parameters will enable optimal performance in the fibrous, diffuse properties of inflated lung. However, the needle design parameters in Table 3.1 show promise for increasing the steerable workspace of the needle in comparison to original needle designs. Step-by-step instructions on manufacturing the flexure-tip needle are included in the Appendix.

Table 3.1: Flexure-tip Design Parameters

bevel	tip length	cut width	cut depth	flexure angle	force to kink	ρ of curvature
10°	8 mm	0.254 mm	70%	38°	0.2 N	84.2 mm

3.2 Increased Aiming Ability: Integrating a Needle-Sized Wrist

We seek high curvature needles, but there will always be a curvature limit. Thus, it is beneficial to include additional degrees of freedom to make sure that the needle is initially aimed in the right general direction, such that the target is within the needle's workspace. To accomplish this, we use a tendon-actuated, bendable outer tube called a wrist in our system. This design was first proposed for use as a distal wrist for needle-sized surgical robots in [58].

Manufacturing of the wrist was accomplished by machining slots to provide flexure points in the material. A thin wire tendon is attached to the distal end of the wrist and variable curvature is achieved by pulling on the tendon attached at the distal end of the slotted tube.

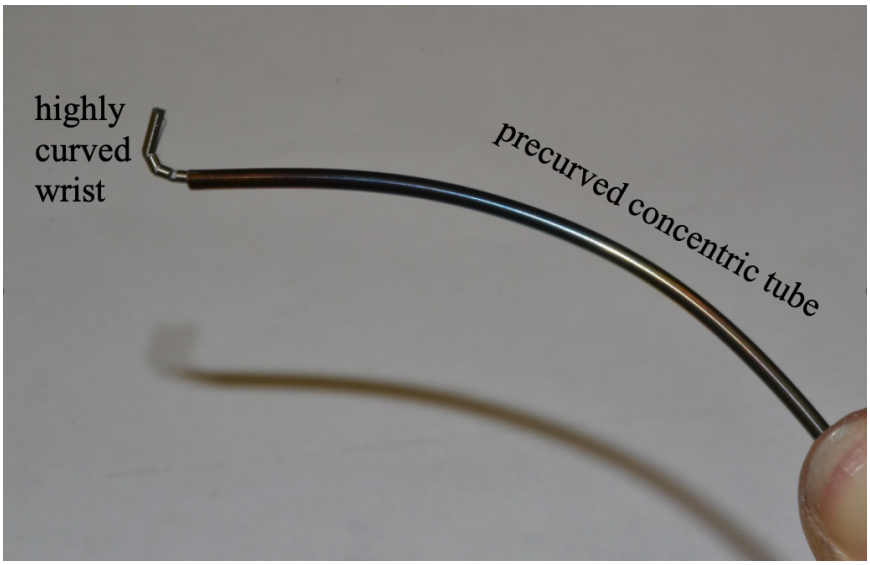

Figure 3.5: A highly curved wrist provides local angular control of bevel tip needle launch angle at the tip of a precurved tube.

Reducing the footprint of the tendon attachment to the distal section of the wrist is crucial for clearance in close, concentric loading of the tool stages. This small-scale attachment is achieved through laser welding the tendon wire to the distal end of the wrist. Tested with a force sensor, we need approximately 20N of force to actuate the wrist with

the steerable needle within its lumen. To achieve this actuation, we use Nitinol wire with a rectangular cross sectional area to enable higher strength in tension. A rectangular profile nitinol wire of dimensions 0.128 mm x 0.356 mm can withstand forces up to 67N (calculated using ultimate tensile stress of nitinol 1070MPa). With the over-design of the actuators presented in section 2.3, we are still well within torque capabilities to achieve this actuation. The bendable section of the wrist is 7.43 mm long and can provide variable bending actuation for aiming the needle stage.

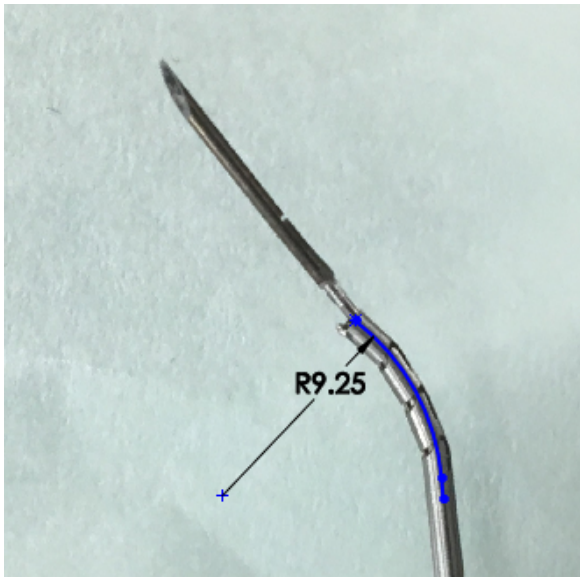

Figure 3.6: Needle-sized wrist capable of actuating the flexure-tip needle at a radius of curvature $<$10 mm

Described in detail in [58], the kinematics of the wrist in free space is determined by the number of slots machined into its wall, which act as a hard stop to its bend upon actuation of its tendon. In our system, we limit the actuation of wrist according to a radius of curvature of 10 mm. This curvature constraint was experimentally determined as the most that the needle inside the wrist can withstand without introducing high friction and corresponding torsional windup in the steerable needle. For comparison, the system of Swaney et al. [44] featured a pre-curved tube with a curved section 27 mm long and a radius of curvature of 17.8 mm. Our new design enables localized curvature of 10 mm along a length of 7.43 mm, and provides variable curvature through tendon actuation. The integration of this wrist as

the second concentric stage enables superior targeting of the steerable needle, providing an increase in the effective targeting workspace of the system.

3.3 Outer Curved Tube

Thus far, we have discussed progress toward increasing the system's steerability through (1) the flexure-tip steerable needle and (2) a variable-curvature wrist stage to orient the needle. Before these two stages are deployed into the parenchymal space, they need to pass out of the airway and into the parenchyma. Consistent with the previous system, an outer concentric tube stage is used to position the wrist prior to its deployment. Our outer tube stage has a radius of curvature of 30 mm, which we determined as the minimum radius of curvature achievable while avoiding plastic deformation of the nested inner tube. This stage completes a three-stage tool assembly, using seven degrees of freedom manipulated by the robotic unit. The tool assembly lies nested within a standard plastic clinical sheath shown in Figure 3.1, and is manually deployed when the targeting of the steerable needle is achieved, acting as a stationary extended working channel once the tools are removed.

In Chapter 3 we present the new designs of the flexure-tip steerable needle and wrist stages of the system. Section 3.1 explores improving the flexure-tip steerable needle to achieve high curvature in porcine tissue, section 3.2 presents a new design for the second concentric tube stage to increase the targeting workspace of the needle, and section 3.3 describes the outermost stage of the system. In Chapter 4, we describe the final design of the actuation unit, catered to the specifications in Chapter 2 and used to control the components detailed in Chapter 3.

Chapter 4

Actuation Unit Design

4.1 Design Description

A compact actuation system was developed to deliver and control the multi-stage transbronchial concentric tube/needle device described in Chapter 3. The actuation unit, shown in Figure 4.1, features four slim carriages, each with the ability to control the rotation and translation of one tube or needle.

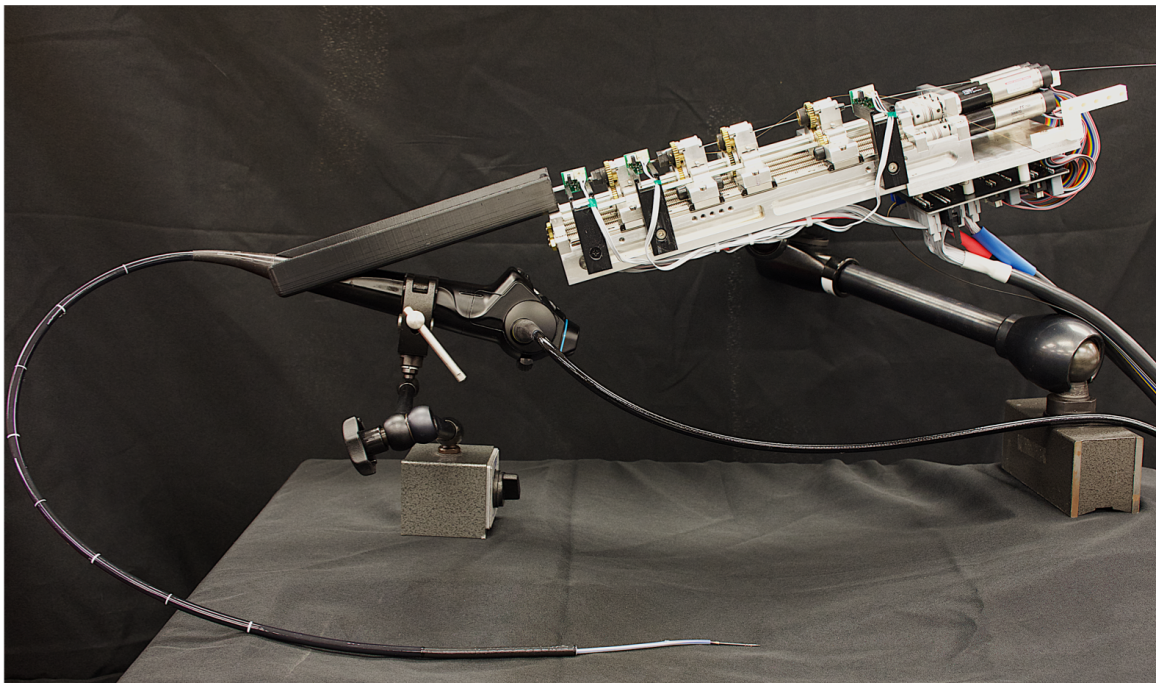

Figure 4.1: The new actuation unit design, shown coupled to the bronchoscope and mounted on a passive arm.

As labeled in Figure 4.2, the carriage closest to the motors is fitted to provide translation of rotation of the steerable needle stage. The middle carriages, labeled as "wrist pull wire" and "wrist" in the figure, are coupled in rotation to prevent windup of the tendon in rotation, but have the ability to translate independently, enabling articulation of the wrist described in section 3.2. For this stage of the system, the robot actuates three degrees of freedom to

achieve variable targeting. The fourth carriage supplies translation and rotation to the outer curved tube stage. Incorporating tendon-actuation with the translation and rotation stages, our new design features seven degrees of freedom.

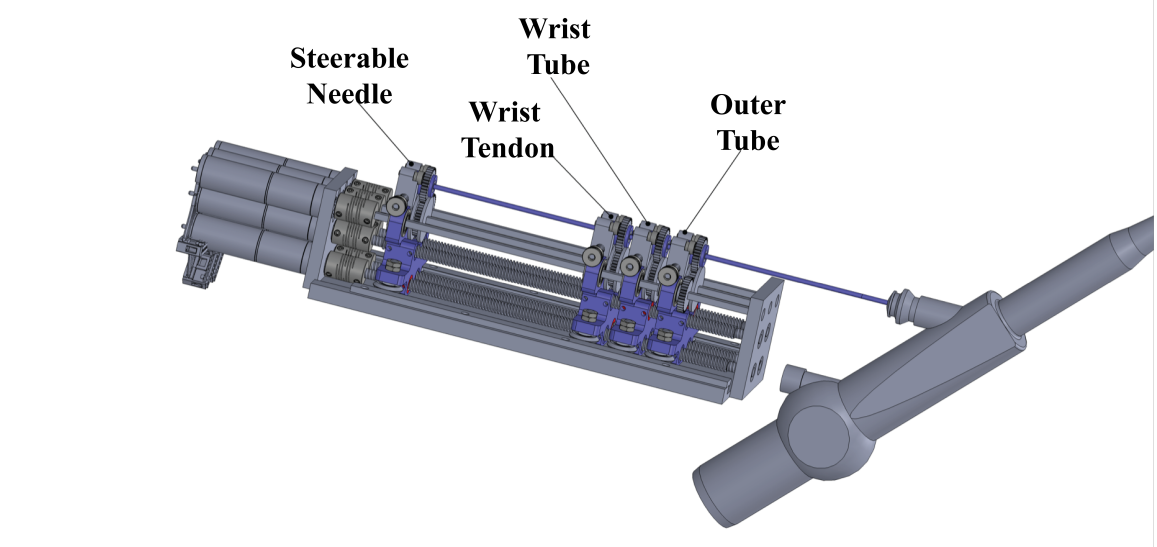

Figure 4.2: Carriages on the mechanical unit are fitted to actuate the steerable needle, wrist tendon, wrist tube, and outer tube stages.

Motors for actuating each degree of freedom are outfitted with planetary gearsets and optical encoders, and are mounted onto the back end of the unit. Rotational motion is transmitted through a geared square shaft (which engages with a spur gear attached to the tool for rotation) and translational motion is transmitted to each tool via a leadscrew (which translates the tool carriage on low-friction linear guiderails).

The high-stiffness chassis is machined from aluminum, and the entire system can be mounted onto a lockable arm (Noga Engineering, Israel) for passive positioning prior to or during the procedure. The design achieves the goal of compactness at 11” long, 4” wide, and 2.5” tall, and its lightweight aluminum chassis is easily maneuvered on a positioning arm. In addition to achieving the design goals of compactness, this design includes a novel coupling mechanism between tools and the transmission unit, achieving modular design.

4.2 Quick-Connect Mechanism

A challenge in designing continuum, endoscopic robots for clinical use involves how the tools are attached to their actuators. Approaches described in literature for attaching the tubes to the actuation unit include gluing the tubes into the mechanism [60, 32, 33, 61], set screw tube adaptors [62], split clamps [34], collet mechanisms [63], and hubs held in place by removable retaining bars [60]. The ability to rapidly and easily interchange various tools as desired is an important capability of this system that has not been realized in prior systems. This modularity can be exploited to configure the system in a way that is best for the particular lesion being targeted, as additional modules (e.g. additional concentric tubes) can be added to increase dexterity as needed. Each tool is pre-configured with an attached spur gear, and can be quickly inserted into or removed from its carriage.

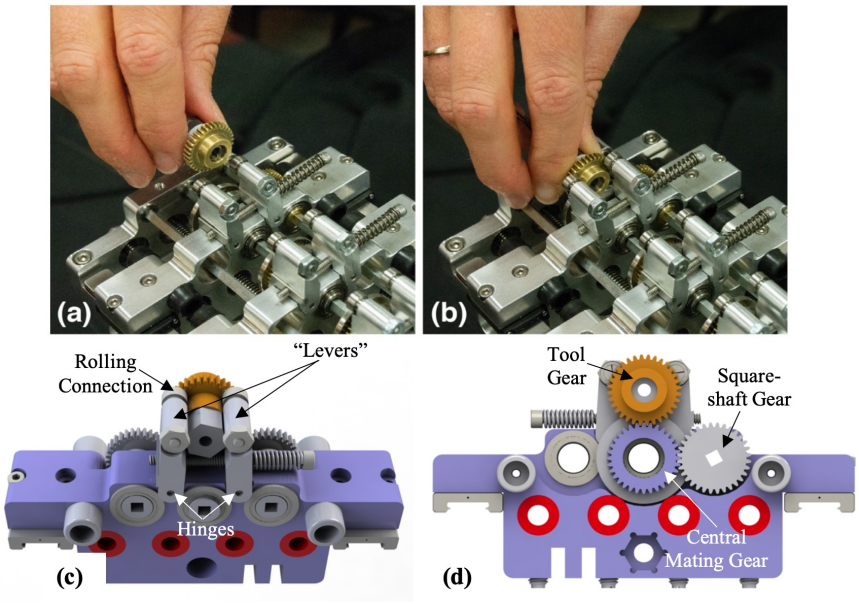

Figure 4.3: Tool quick-connect mechanism: *(a)* before and *(b)* after the tool gear is inserted. *(c)* CAD rendering of the top view of the lever mechanism with *(d)* showing gear engagement.

The mechanism, shown in Figure 4.3, features two spring-loaded levers which deflect to accept the spur gear hub, and retract to couple the gear hub between two rolling elements (one on each lever) and the mating gear mounted on the carriage. The spur gear on the tool

meshes with the central mating gear on the carriage, enabling the transmission of rotational motion from the square shaft.

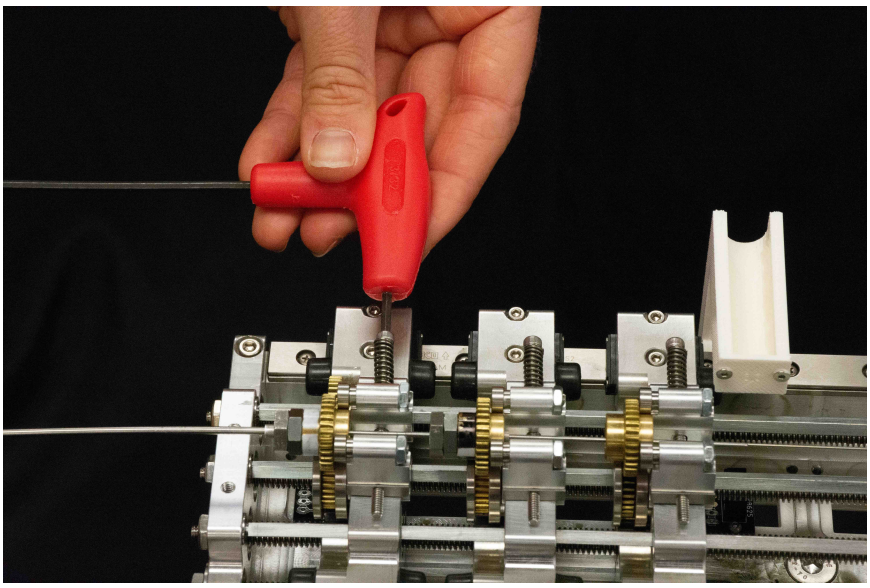

Figure 4.4: The pre-load of the spring-loaded levers can be adjusted with a set screw before tool loading.

The spring tension between the levers can be adjusted, thereby altering the pre-load as shown in Figure 4.4 between the tool gear and the mating carriage gear, to minimize backlash.

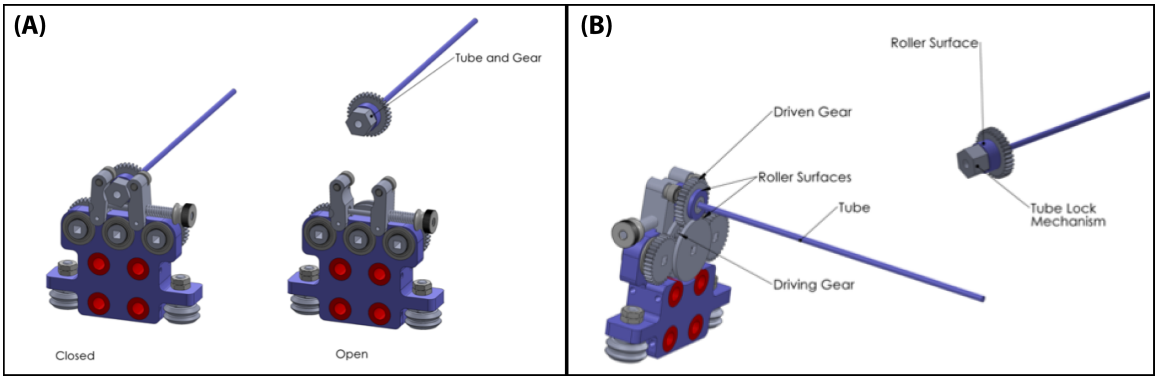

Figure 4.5: The quick-connect mechanism depicted in closed and open configurations for tube loading in (*A*), rolling contact surfaces and collet connecting the tube to the gear in (*B*)

Shown in Figure 4.5 (*B*) as a tube lock mechanism, tubes are grasped by ShaftLoc sleeves (SPD/SI), which carry a small, drilled adaptor to which the back end of the tube

is adhered or press fit to. The ShaftLoc sleeve expands into the inner lumen of the gear while constricting onto the adaptor and tube when tightened. Mini adaptor chucks (Gyros Precision Tools, 14 Melnick Dr, Monsey, NY 10952) adhered to the gear are used for the smaller (0.5mm scale) tubes and enable easy replacement of the steerable needle tube. The tool/gear design is catered towards the tubes with their attached gears being disposable, though future work is needed on a bagging concept for the actuation unit, which may change the interface design. This novel design enables tools to be loaded individually, or coupled as a unit to their respective carriages.

4.3 Fail-Safe Feature

The translation of each carriage features a fail-safe feature, which has been useful in development of the hardware. If a motor responsible for translation transmits uncontrolled power to a carriage and a high-force collision between carriages occurs, the carriage is suddenly disengaged from the lead screw and the responsible motor. This prevents stall or damage to the motor from occurring. In a clinical scenario, this fail-safe feature accounts for any unanticipated high forces transmitted from the needle to the actuation unit, causing the actuation unit to disengage.

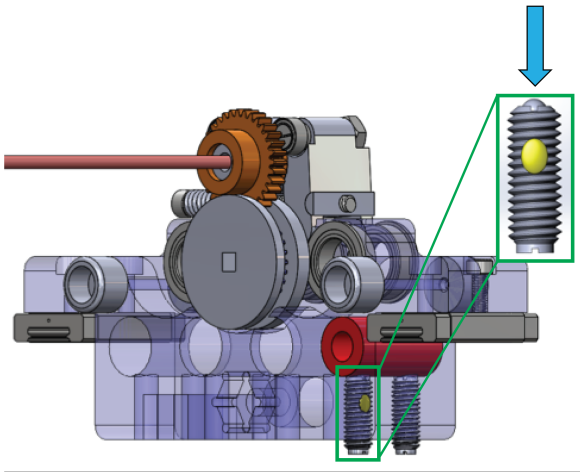

Figure 4.6: CAD model featuring a transparent purple carriage and ball-nose spring plungers used to load the red lead screw nut into the carriage. The ball-nose of the spring plunger shown in the inset depresses at forces caused by collision, releasing the red lead screw nut and disengaging the carriage from further translation.

The fail-safe feature is achieved by using slotted ball-nose spring plungers (McMaster-Carr, 1901 Riverside Pkwy, Douglasville, GA) depicted in the green inset of Figure 4.6, to load the lead screw nut (shown in red in Figure 4.6) into the carriage. When a force of $\geq$ 5lb is applied to the ball-nose spring plunger, it depresses, and the lead screw nut disengages from the carriage assembly. The carriage is left stationary while the lead screw nut travels forward on the lead screw. This fail-safe design enables easy reconstruction of the carriage and lead screw assembly in the event of a high-force collision and provides additional time to cut power to the responsible motor. This safety feature has been useful in development and can translate into the clinical setting to protect against anything causing unanticipated forces at the end effector end during procedure.

4.4 Incorporating Homing Sensors

The new design features optical sensing technology to ease operation. An important aspect of making a practical robot of this type for the operating room is developing a specific technique for homing, or returning the tubes to a known location (home position) on the robot. Since high resolution motor encoders are typically incremental, an initializa-

tion routine is necessary for the robot to know precisely where each carriage (and hence each tube's home position) is in both linear insertion and axial rotation degrees of freedom. When the robot is first turned on, this ability to establish absolute positions and orientations of the tools is particularly useful for ease and accuracy in bench-top experimentation environments. Additionally, added precision in tool locations lends itself to the clinical setting during registration. Registration errors and uncompensated tool offsets can lead to false-negative biopsy results and misdiagnoses [64], especially for small ($<$ 10mm) peripheral nodules. Tactile, snap-action limit switches are a viable approach [31], but require wires to move with carriages in the actuation unit, which introduces a potential failure point. The new design features a method for integrating optical sensors in a way that eliminates the need for moving wires.

We designed a precise, systematic homing protocol to establish a repeatable home position for the robot using optical sensors to sense the absolute rotational and translational configurations of each tube relative to fixed locations on the the actuation unit. Optical photointerruptors (OPB625, TT Electronics) are responsible for translational homing, and are built into the stationary chassis of the actuation unit, one for each carriage. Circuitry was designed to relay the logic output of the photointerruptor to the translational motor responsible for the movement of a carriage. These trigger when a protrusion on the carriage breaks the optical path of the sensor, indicating the "home position" has been reached.

Rotational reflective sensors (OPB608V Reflective Sensor, TT Electronics) are placed on plastic support arms mounted to the chassis so that they align with the gear hub when the translational sensor is triggered (Figure 4.7), and a reflective homing mark on the gear hub indicates the rotational home position. Circuitry relays the analog signals of the reflective sensors to logic outputs directed to each rotational motor. The homing protocol, which initiates upon system power-up, is carried out as follows: (1) each carrier is retracted until the chassis-mounted translational sensor associated with that carriage is activated, establishing a home position on the linear axis, (2) the rotational degree of freedom is advanced

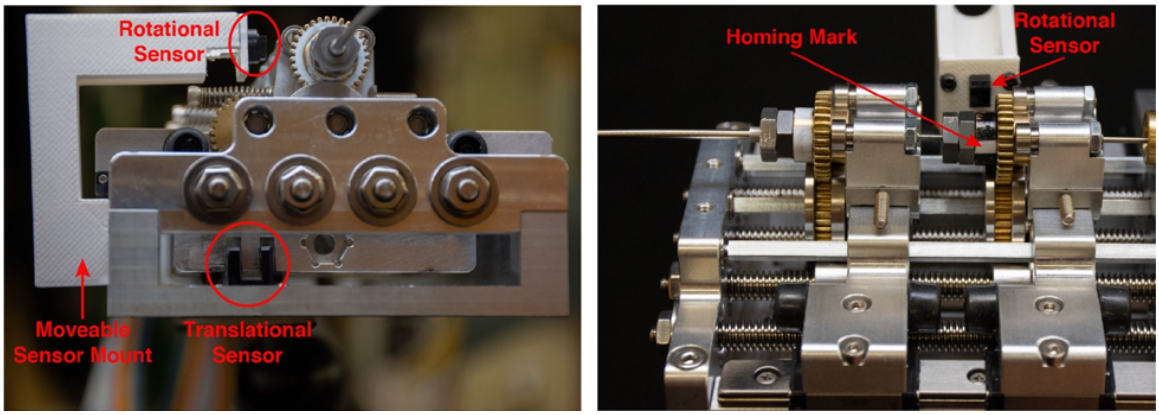

Figure 4.7: Homing sensors: *(left)* front view of the actuation unit showing the placement of the rotational and translational sensors, *(right)* side view of the actuation unit showing the reflective fiducial.

unidirectionally until the chassis-mounted rotational sensor is triggered (Figure 4.7(right)), thereby establishing home position on the rotational axis.

To quantify the accuracy of the homing protocol, we conducted 12 repeatability tests on each axis. For each test, homing was executed, and the incremental encoder readings for translational and rotational motors were recorded once the system had arrived at its home position. Our system's encoders provide a linear resolution of 0.021 μm and an angular resolution of 0.0021°. Homing precision was measured to have a standard deviation of $\pm$7.3 μm (maximum difference 25.3 μm) and $\pm$0.09° (maximum difference 1.67°), for translation and rotation, respectively. Whereas previous methods of homing included visual alignment of markers, these homing sensors provide precision in orienting our tools, allowing for efficient, repeatable experimentation. In homing our tools stages, we are able to achieve repeatable positions to the μm level, and orientations within 1-2°.

In Chapter 4 we described the mechanical design of a compact robotic actuation unit for peripheral lung biopsy. It is modular in the sense that the tools can be easily decoupled from the actuation unit, and is oriented towards clinical workflow requiring quick-loading or tool changes. Fulfilling design goals and specifications, the mechanical unit incorporates homing sensors to enable rapid, repeatable initial positions for all stages. In Chapter 5,

we validate the designed system with accurate closed-loop needle steering, and conduct experiments using targets identified in preoperative imaging.

Chapter 5

Experimental Results

The compact actuation system described in the Chapter 4 will deploy a steerable needle and the concentric tube stages used to aim it through a bronchoscope port, with the goal of enabling accurate and safe access to peripheral lung lesions. Our system uses electromagnetic tracking combined with imaging information to accurately steer through lung tissue to the physician's desired target. To demonstrate the capabilities of our new actuation unit, we performed accuracy targeting experiments with the steerable needle stage steered to virtual targets in phantom tissue. We then performed a second experiment in which target points were selected in CT images.

5.1 Closed-Loop Needle Steering: Benchtop Experiments

We have previously demonstrated steering to targets using a rapid replanning framework [65] and via sliding mode control described by Rucker et al. [28]. In this system, we use the sliding mode controller with constant insertion and rotational velocity inputs to target a point in space. The controller dynamically regulates the insertion and orientation of the steerable needle at each control loop by aligning the curvature plane of steerable needle with positional error vector while inserting the needle continuously. It is a robust, effective and computationally efficient control strategy for this application, and does not rely on any model parameters (such as needle curvature) to reliably converge. The experimental setup is shown in Figure 5.1. The sliding mode controller was implemented via the Robot Operating System (ROS). We used this system to target lesions embedded in phantom tissue made from synthetic ballistics gel (Humimic Medical, Fort Smith, AR). The flexure-tip steerable needle described in the experiments is of the design described in section 3.1, featuring a shaft of 0.57mm OD superelastic nitinol tube. The tip (in which the tracking coil was em-

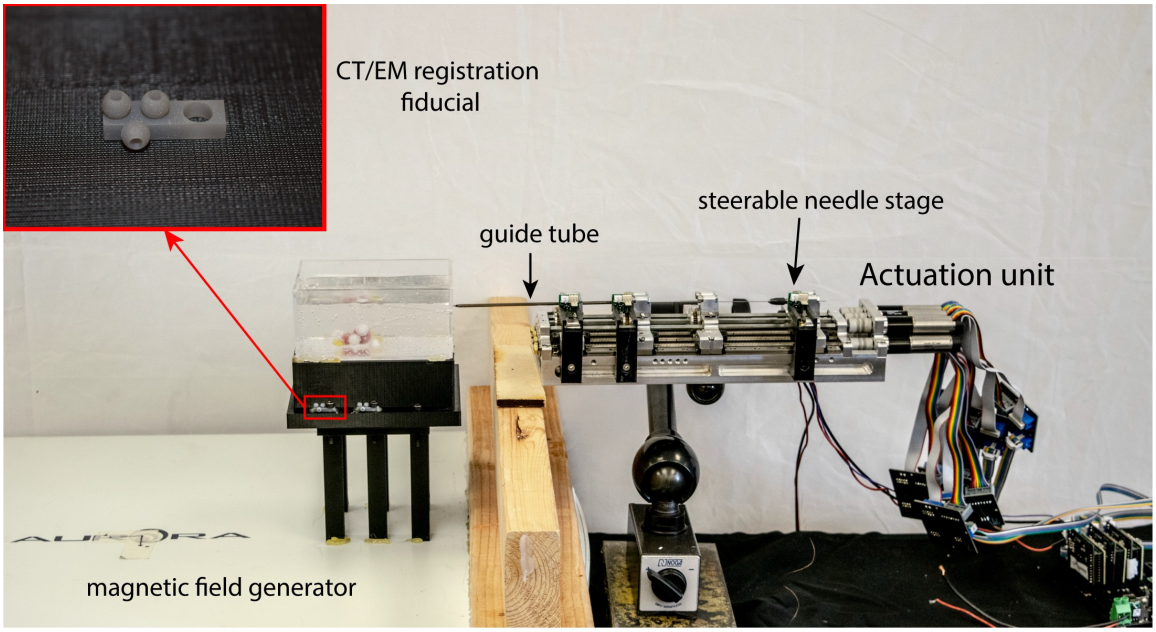

Figure 5.1: Experimental setup for closed-loop needle steering and lesion targeting, where the inset shows an enlarged view of the fiducial markers.

bedded) was made from a short length of 0.80 mm nitinol tube with a flexure hinge and a 10° bevel tip. A 0.41mm diameter, 5-DoF magnetic tracking coil (Northern Digital Inc., Canada) was embedded in the steerable needle tip, and the 6th degree of freedom (rotation about the needle axis) was inferred from needle base angle. The position and orientation data from the sensor tip was fed into the sliding mode controller to update the current pose at each iteration with a rate of 35 Hz for closed-loop control.

The closed-loop targeting performance of the system was verified in the ballistics gel phantom mentioned previously. This experiment was done on the benchtop in the lab with magnetic tracker feedback. Eight different target points within the steerable needle's workspace were selected, and the needle was steered to each using the sliding mode controller. As shown in Figure 5.2, the controller was able to steer the needle to the target points successfully. The mean error between final needle tip positions and target points was 0.46 mm $\pm$0.28 mm (maximum 0.96 mm). This accurate targeting demonstrates our system's ability to perform the crucial task of targeting small nodules. Note, this accuracy will likely not reflect the final accuracy of the system, with errors expected from imaging

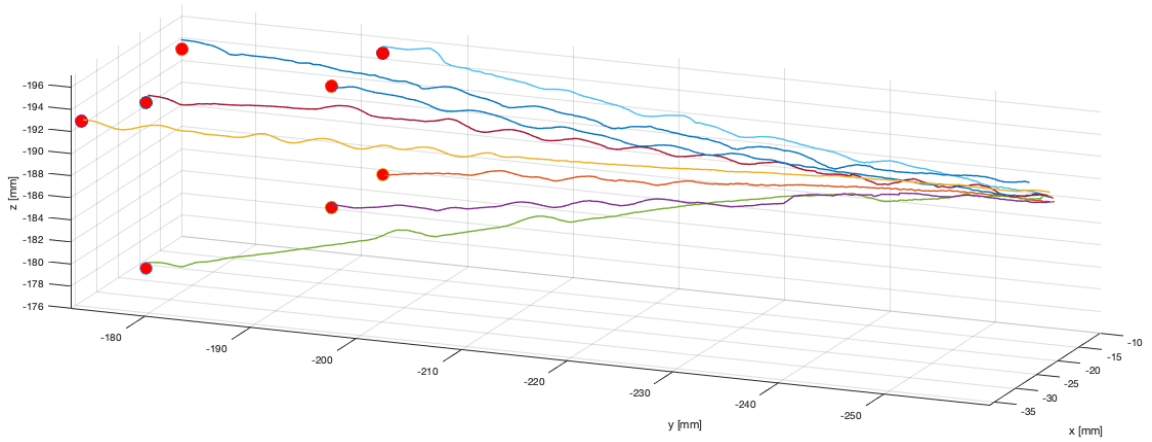

Figure 5.2: Benchtop needle steering experimental needle tip paths, as measured by the magnetic tracker embedded in the needle's tip. The target points selected in magnetic tracker space are indicated by red spheres. Data points in the traces above are spaced approximately 78 μm from one another, and a 25-point moving average was used to filter sensor noise prior to plotting. The slight wobbles in the traces indicate times when the closed loop controller re-oriented the flexure-tip needle (the tip of the bevel is plotted).

registration and intraoperative movement of the targets from breathing motions. However, with an accuracy of half a millimeter, the combined potential of the new actuation unit design and a steerable stages is promising.

5.2 Closed-Loop Needle Steering: In CT Scanner Experiments

After demonstrating closed-loop needle steering performance for virtual targets placed in the phantom, the system was tested for its ability to target nodules derived from a preoperative CT scan. Spherical objects simulating lung lesions were embedded in the ballistics gel phantom. The phantom was scanned using a CT scanner (Xoran Technologies, USA) to determine the location of these lesions in CT space. Twelve fiducial markers attached to the phantom (as shown in the inset in Figure 5.1) were used to determine the homogeneous transformation matrix $\mathbf{T} \in \mathbb{R}^{4\times4}$ between CT space and magnetic tracker space. We segmented the spherical targets from the CT to obtain their positional coordinates, and transformed their locations into magnetic tracker space. The steerable needle was steered

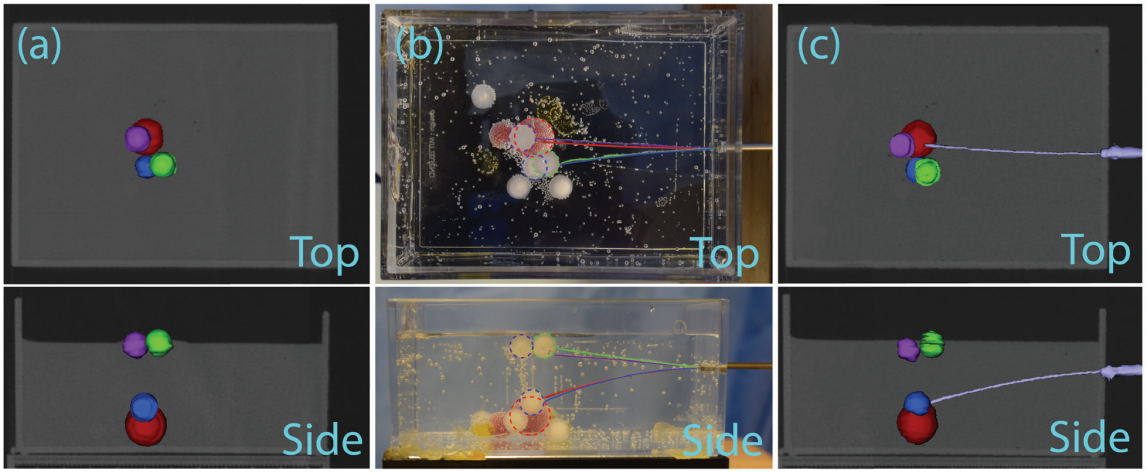

Figure 5.3: Experimental results for the lesions targeted from pre-operative CT scan: *(a)* top and side views of the reconstructed pre-operative CT scan of the phantom with the four target lesions segmented: 9.5 mm diameter plastic spheres are shown in purple, blue, and green, and a 13 mm diameter silicon sphere is shown in red, *(b)* top and side views of the needle tip trajectories shown in the phantom, where each trajectory is indicated by the color of its corresponding target lesion, *(c)* an example post-operative reconstructed CT image displaying the needle successfully reaching the far red lesion.

to hit these targets using magnetic tracker feedback (just as in the benchtop experiments) and the final error was assessed using a post-insertion CT scan. Four simulated lesions were targeted as shown in Figure 5.3, and all were hit successfully with the needle.

The paths followed by the needle to each lesion are shown in Figure 5.3 (b). The needle path and lesions segmented from the postoperative CT images are shown in Figure 5.3 (c) for one of the lesions targeted. Since the target lesions used in these experiments were rigid compared to the surrounding tissue, we did not attempt to push the needle tip inside them, to avoid damaging the tip, instead stopping the needle at the surface of the lesion. Based on this, we confirmed that the needles hit each desired lesion, but did not compute a final tip accuracy in CT space. These results illustrate that the robotic system is able to accurately target lesions identified in CT images.

These targeting experiments validate our robot's ability to deploy the steerable needle and accurately target lesions identified in preoperative imaging. With targeting accuracies under 0.5mm in benchtop testing, the system has great potential in the clinical setting. The

steerable needle targeting will be augmented with a bronchoscope, concentric tube aiming stages, and motion planning software to yield full system deployment into the peripheral lung.

Chapter 6

Future Work and Conclusions

6.1 Future Work

The combination of concentric tube, needle-sized wrist, and steerable needle technologies holds significant promise as a peripheral targeting system to extend the reach of transoral bronchoscopy. The work presented in this thesis has advanced the system several steps closer to the real-world operating room, while also identifying areas of further development which will be useful to translate this system into the clinical setting.

6.1.1 Hardware: Steerable Needle Optimization

Improvements to the slotted flexure-tip design have enabled high curvature steering in porcine loin and ex vivo deflated lung, but there remains room to optimize this design for steering within perfused, inflated lung. Optimization can be performed by varying the flexure hinge parameters: cut depth, cut width, bevel angle, location of the flexure hinge, as well as needle shaft stiffness, all of which combine with tissue properties to define the achievable needle curvature. While previous work on bevel-tip needles has shown that smaller bevel angles trend toward increased curvature [53], in the case of the flexure-tip needle, changing the bevel angle appears to have a small effect on needle curvature relative to that of other design parameters. The cut width and cut depth parameters jointly influence the angle and stiffness of the flexure hinge. The angle of the flexure hinge has a great effect on the achievable curvature of the needle. If it is too small, the needle will behave as a standard bevel-tip needle; if it becomes too large, however, it becomes impossible to steer in tissue. This implies that there is some optimal flexure angle between 0° and 90° which may be specific to the tissue and the other needle parameters used. The stiffness of the flexure angle is primarily important as a design constraint; at high cut widths and depths,

the stiffness of the joint may decrease so much that there is a risk of the tip breaking off within the tissue. While the combination of cut depth and cut width that produces an optimal flexure angle and stiffness for steering in perfused lung tissue remains to be found, we have found that cut widths of approximately 25% and cut depths of 70% of the OD of the needle tip produce flexure joints that perform well in deflated, ex vivo lung tissue. To choose the location of the flexure hinge, we noted that needle steering performance is sensitive to tip length. Previous work shows that larger tip lengths enable increased curvature in kinked-tip needles [52, 59]. To this end, we chose the location of the flexure joint to be just behind the sensor, to leverage a long tip length of 8 mm. This provides the additional benefit of tracking the location and orientation of the needle tip, rather than tracking a point more proximal within the shaft, which is useful for controller performance.

The flexibility constraint of the needle shaft will be identified by testing needles of reduced moment of inertia, with the goal of finding the least stiff needle that remains stiff enough to avoid buckling within lung tissue, as decreasing stiffness will maximize the achievable needle curvature during insertion. Finding needle parameters to enable high curvature performance can be accomplished experimentally, by testing various designs in inflated lung tissue, and measuring their curvature upon pure insertion into the tissue through CT imaging to visualize the path of curvature. Toward optimizing for lung tissue, we will further compare parameter ranges by using precise wire electric discharge machining (EDM) manufacturing for more accurate fabrication and comparison of these small-scale designs. The optimal stiffness of the needle shaft can first be explored using cost-effective Nitinol wire of varying diameter, and equated to tubing of equivalent inertial properties.

6.1.2 Hardware: Bronchoscope Loading

A minor challenge associated with this system is loading the tool assembly through the angled tool port of the bronchoscope. Current diagnostic and therapeutic bronchoscopes

feature a 45° bend inside the handle, which requires bending the tools with high curvature in order to pass them into the working channel. This becomes problematic for larger diameter or stiffer tubes, which can plastically deform when passed through the bend of the tool port.

We have addressed the challenge of bronchoscope loading in two ways throughout this work. First, we have sought to reduce the overall stiffness of the tools passed through the port in comparison to prior designs, which required loading the tools from the tip of the bronchoscope to avoid plastic deformation of the tool tips [44]. As such, an objective throughout this work has been to minimize the diameter of the needle and all tubes, subject to the constraint that the tubes remain stiff enough to avoid buckling within lung tissue. We have made progress toward this goal by reducing the size of the needle tip from 1.16 mm [44] to 0.8 mm and finding methods to reduce the footprint of the tendon attachment of the wrist in comparison to prior designs. The wrist tendon and its attachment to the wrist tube adds to the overall diameter of the device, but precise laser welding of the tendon to the wrist tube reduces this diameter increase in comparison to prior prototypes, which involved looping the tendon through the distal slot of the wrist.

Second, we have altered a commercial bronchoscope to reduce the bend angle in the tool port, allowing for easier insertion of the tools into the working channel. We demonstrated this solution by machining the plastic port of the bronchoscope to remove some length of the insertion channel, reducing the overall angle of the tool port, while preserving the internal tendons for tip articulation. This enabled us to achieve loading into the bronchoscope with a 22° bend, as shown in Figure 6.1, reducing the insertion angle by 50%.

Future improvements can be made on both of these fronts in order to further reduce the challenges of loading tools into the bronchoscope. As demonstrated by our ability to machine the tool channel into a different angle without interfering with the functionality of the device, the 45° bend in the working channel is not an inherent design requirement for a tendon-actuated bronchscope. Thus, future partnerships with commercial bronchoscope

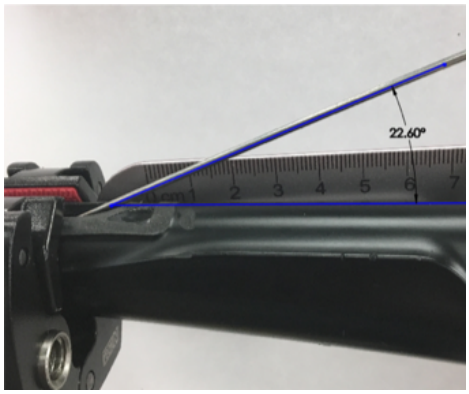

Figure 6.1: Machined bronchoscope loading at 22°

manufacturers can open the door to eliminate this loading problem altogether, by using custom endoscopes with straight or nearly straight working channels. In addition, further design optimization of each tool, coupled with the manufacturing of custom nitinol tubes, is a promising direction for achieving tools which are flexible enough to load through the port of a standard bronchoscope.

6.1.3 Hardware: Clinically-Ready Robot

While sterility methods were considered in the design of this robotic system, fully addressing this challenge and experimentally validating the solution is left to future work. The quick-connect tool loading of the current design lends itself toward a workflow in which the tools can be disposable and couple through a sterile barrier to a reusable actuation unit. This sterility method is currently used in the da Vinci surgical system [66] and a similar concept has been demonstrated for concentric tube robot systems designed for transnasal surgery [67]. We see this sterility method as having promise for convenient integration into existing clinical practices, and fabrication of this concept should be a design goal of future prototypes.

6.1.4 Software: Steerable Needle Controller

The system requires a method to measure or estimate the axial "roll" angle about the needle's tip axis, which may differ from the angle input at the needle's base due to friction-induced torsional windup. In the past, a 6-DoF sensor was used to provide the full needle pose in closed-loop control [44]; however, currently available 6-DoF tracking coils are too large in diameter to embed within the needle tips used in this work. In our experiments, we used a small, 5-DoF magnetic tracking coil to enable closed-loop control, estimating the roll degree of freedom by directly using the angle input by our rotational actuator at the needle's base. This is equivalent to assuming that the needle is torsionally rigid. While this assumption was acceptable for initial experiments using a short-length needle, a longer needle passed through the bronchoscope will likely increase the amount of torsional windup. To estimate this last degree of freedom without the need for a large 6-DoF sensor, we plan to use a Kalman filtering approach [68] or an observer-based approach [69] in the future.

6.1.5 Software: Breathing Compensation

Lastly, we will build on the steerable needle targeting experiments presented in Chapter 5 to better simulate the real clinical scenario. This system is intended for use in breathing patients, and accounting for target motion during respiration will present new challenges to accurate steerable needle targeting. Electromagnetic navigation systems currently exist to measure patient breathing motion, by registering electromagnetic fiducials on the patient's body to instances of full inspiration and expiration lung volume. Motion from respiration can then be measured by interpolating between fiducial movement [18]. Similar methods to compensate for target motion, or control breathing patterns, are being investigated in [26] as viable avenues to solve this challenge. Future studies will feature deployment of the full tool assembly in live animal studies to characterize the accuracy of our system as intended in the clinical setting.

While there remains work to be done before this system is ready for use in patients, this thesis has identified several major areas which were left to future work by prior systems and presented solutions which bring the platform closer to a practical clinical system. Towards hardware development, we have a clear path to optimize the needle for steerability in perfused, ventilated lung tissue, and have identified solutions to enable the loading of instruments in the working channel of the bronchoscope. The actuation unit enables rapid tool changes which will be highly useful in a future clinical version of the robot, which also addresses the sterility of the system. Towards software development, we have identified solutions to estimate the 6^{th} degree of freedom for accurate steerable needle sensing, and avenues to compensate for respiration as expected in the clinical setting.

6.2 Conclusion

In this body of work, we presented new developments to a robotic system that provides the safety of transoral approaches with the peripheral access of percutaneous approaches. We have taken important steps toward clinical translation of this system by creating a completely new second generation prototype. We have explored the clinical application in order to develop a comprehensive set of functional requirements which were used to drive the design of the robot and its various components. Advances to end effector design of the robotic system increase the effective workspace of the system through flexure-tip needle enhancements, as well as the incorporation of a wrist stage, both of which improve targeting ability in the peripheral lung. The mechanical design of the actuation unit is compact, with modular tool change capability enabling a workflow-oriented system. The actuation unit incorporates homing sensors to facilitate ease of use in experiments, and safety features useful to transition into the clinical setting. Our system has the ability to achieve steerability and obstacle avoidance in the lung parenchyma, while integrating smoothly with existing imaging and navigational modalities. These are capabilities that commercially available systems do not provide, extending the reach of bronchoscopy to small, peripheral lung nodules. With

this system, we take important steps toward giving physicians the reach they need in order to safely diagnose and combat cancer at its earliest stages.

BIBLIOGRAPHY

[1] Robert A Smith, Kimberly S Andrews, Durado Brooks, Stacey A Fedewa, Deana Manassaram-Baptiste, Debbie Saslow, Otis W Brawley, and Richard C Wender. Cancer screening in the united states, 2018: a review of current american cancer society guidelines and current issues in cancer screening. *CA: A Cancer Journal for Clinicians*, 68(4):297–316, 2018.

[2] National Lung Screening Trial Research Team. Reduced lung-cancer mortality with low-dose computed tomographic screening. *New England Journal of Medicine*, 365(5):395–409, 2011.

[3] Ferris M Hall. Identification, biopsy, and treatment of poorly understood premalignant, in situ, and indolent low-grade cancers: are we becoming victims of our own success? *Radiology*, 254(3):655–659, 2010.

[4] Ronald S Winokur, Bradley B Pua, Brian W Sullivan, and David C Madoff. Percutaneous lung biopsy: technique, efficacy, and complications. In *Seminars in interventional radiology*, volume 30, page 121. Thieme Medical Publishers, 2013.

[5] Nishita Kothary, Laura Lock, Daniel Y Sze, and Lawrence V Hofmann. Computed tomography–guided percutaneous needle biopsy of pulmonary nodules: impact of nodule size on diagnostic accuracy. *Clinical lung cancer*, 10(5):360–363, 2009.

[6] Aykut Recep Aktaş, Emel Gözlek, Ömer Yılmaz, Mustafa Kayan, Nisa Ünlü, Hakan Demirtaş, Bumin Değirmenci, and Mustafa Kara. Ct-guided transthoracic biopsy: histopathologic results and complication rates. *Diagnostic and Interventional Radiology*, 21(1):67, 2015.

[7] Kee-Min Yeow, I-Hao Su, Kuang-Tse Pan, Pei-Kwei Tsay, Kar-Wai Lui, Yun-Chung Cheung, and Andy Shau-Bin Chou. Risk factors of pneumothorax and bleeding:

multivariate analysis of 660 ct-guided coaxial cutting needle lung biopsies. *Chest*, 126(3):748–754, 2004.

[8] Jessica S Wang Memoli, Paul J Nietert, and Gerard A Silvestri. Meta-analysis of guided bronchoscopy for the evaluation of the pulmonary nodule. *Chest*, 142(2):385–393, 2012.

[9] Jonathan Lorenz and Matthew Blum. Complications of percutaneous chest biopsy. In *Seminars in interventional radiology*, volume 23, page 188. Thieme Medical Publishers, 2006.

[10] Lucas Fiore, Nathan Elie Frenk, Guilherme Lopes Pinheiro Martins, Publio Cesar Cavalcante Viana, and Marcos Roberto de Menezes. Systemic air embolism after percutaneous lung biopsy: A manageable complication. *Journal of radiology case reports*, 11(6):6, 2017.

[11] Fumiko Kodama, Toshihide Ogawa, Masayuki Hashimoto, Yoshio Tanabe, Yuji Suto, and Takashi Kato. Fatal air embolism as a complication of ct-guided needle biopsy of the lung. *Journal of computer assisted tomography*, 23(6):949–951, 1999.

[12] Prasoon Jain, Sarah Hadique, and Atul C Mehta. Transbronchial lung biopsy. In *Interventional Bronchoscopy*, pages 15–44. Springer, 2013.

[13] Deborah Shure. Transbronchial biopsy and needle aspiration. *Chest*, 95(5):1130–1138, 1989.

[14] Mark G Slade, Najib M Rahman, Andrew E Stanton, Lynne Curry, GC Slade, CA Clelland, and FV Gleeson. Improving standards in flexible bronchoscopy for lung cancer. *European Respiratory Journal*, 37(4):895–901, 2011.

[15] Walid A Baaklini, Mauricio A Reinoso, Arnold B Gorin, Amir Sharafkaneh, and

Prasad Manian. Diagnostic yield of fiberoptic bronchoscopy in evaluating solitary pulmonary nodules. *Chest*, 117(4):1049–1054, 2000.

[16] Alicia N Rodriguez. Flexible bronchoscopy. In *Interventions in Pulmonary Medicine*, pages 13–34. Springer, 2013.

[17] Udaya BS Prakash. Advances in bronchoscopic procedures. *Chest*, 116(5):1403–1408, 1999.

[18] Christopher Gilbert, Jason Akulian, Ricardo Ortiz, Hans Lee, and Lonny Yarmus. Novel bronchoscopic strategies for the diagnosis of peripheral lung lesions: present techniques and future directions. *Respirology*, 19(5):636–644, 2014.

[19] Sandeep J Khandhar, Mark R Bowling, Javier Flandes, Thomas R Gildea, Kristin L Hood, William S Krimsky, Douglas J Minnich, Septimiu D Murgu, Michael Pritchett, Eric M Toloza, et al. Electromagnetic navigation bronchoscopy to access lung lesions in 1,000 subjects: first results of the prospective, multicenter navigate study. *BMC pulmonary medicine*, 17(1):59, 2017.

[20] Ralf Eberhardt, Devanand Anantham, Felix Herth, David Feller-Kopman, and Armin Ernst. Electromagnetic navigation diagnostic bronchoscopy in peripheral lung lesions. *Chest*, 131(6):1800–1805, 2007.

[21] Gregorino Paone, Emanuele Nicastri, Gabriele Lucantoni, Raffaele Dello Iacono, Paolo Battistoni, Anna Lisa D'Angeli, and Giovanni Galluccio. Endobronchial ultrasound-driven biopsy in the diagnosis of peripheral lung lesions. *Chest*, 128(5):3551–3557, 2005.

[22] Felix JF Herth, A Ernst, R Eberhardt, P Vilmann, H Dienemann, and M Krasnik. Endobronchial ultrasound-guided transbronchial needle aspiration of lymph nodes in the radiologically normal mediastinum. *European Respiratory Journal*, 2006.

[23] Felix JF Herth, Ralf Eberhardt, Daniel Sterman, Gerard A Silvestri, Hans Hoffmann, and Pallav L Shah. Bronchoscopic transparenchymal nodule access (btpna): first in human trial of a novel procedure for sampling solitary pulmonary nodules. *Thorax*, pages thoraxjnl–2014, 2015.

[24] Philip J Swaney, Arthur W Mahoney, Andria A Remirez, Erik Lamers, Bryan I Hartley, Richard H Feins, Ron Alterovitz, and Robert J Webster. Tendons, concentric tubes, and a bevel tip: Three steerable robots in one transoral lung access system. In *Robotics and Automation (ICRA), 2015 IEEE International Conference on*, pages 5378–5383. IEEE, 2015.

[25] Philip J Swaney, Arthur W Mahoney, Bryan I Hartley, Andria A Remirez, Erik Lamers, Richard H Feins, Ron Alterovitz, and Robert J Webster III. Toward transoral peripheral lung access: Combining continuum robots and steerable needles. *Journal of medical robotics research*, 2(01):1750001, 2017.

[26] Alan Kuntz, Luis G Torres, Richard H Feins, Robert J Webster, and Ron Alterovitz. Motion planning for a three-stage multilumen transoral lung access system. In *Intelligent Robots and Systems (IROS), 2015 IEEE/RSJ International Conference on*, pages 3255–3261. IEEE, 2015.

[27] Philip J Swaney, Jessica Burgner, Hunter B Gilbert, and Robert J Webster. A flexure-based steerable needle: high curvature with reduced tissue damage. *IEEE Transactions on Biomedical Engineering*, 60(4):906–909, 2013.

[28] D Caleb Rucker, Jadav Das, Hunter B Gilbert, Philip J Swaney, Michael I Miga, Nilanjan Sarkar, and Robert J Webster. Sliding mode control of steerable needles. *IEEE Transactions on Robotics*, 29(5):1289–1299, 2013.

[29] Kevin Cleary and Charles Nguyen. State of the art in surgical robotics: Clinical ap-

plications and technology challenges. *Computer Aided Surgery*, 6(6):312–328, 2001. PMID: 11954063.

[30] Russell H. Taylor, Arianna Menciassi, Gabor Fichtinger, Paolo Fiorini, and Paolo Dario. *Medical Robotics and Computer-Integrated Surgery*, pages 1657–1684. Springer International Publishing, Cham, 2016.

[31] Liao Wu, Shuang Song, Keyu Wu, Chwee Ming Lim, and Hongliang Ren. Development of a compact continuum tubular robotic system for nasopharyngeal biopsy. *Medical & biological engineering & computing*, 55(3):403–417, 2017.

[32] Yifan Zhu, Philip J Swaney, Isuru S Godage, Ray A Lathrop, and Robert J Webster. A disposable robot for intracerebral hemorrhage removal. *Journal of Medical Devices*, 10(2):020952, 2016.

[33] Meysam Torabi, Rajiv Gupta, and Conor James Walsh. Compact robotically steerable image-guided instrument for multi-adjacent-point (map) targeting. *IEEE Transactions on Robotics*, 30(4):802–815, 2014.

[34] Tania K Morimoto, Elliot Wright Hawkes, and Allison M Okamura. Design of a compact actuation and control system for flexible medical robots. *IEEE robotics and automation letters*, 2(3):1579–1585, 2017.

[35] Michael H Loser and Nassir Navab. A new robotic system for visually controlled percutaneous interventions under ct fluoroscopy. In *International Conference on Medical Image Computing and Computer-Assisted Intervention*, pages 887–896. Springer, 2000.

[36] Ulrich Hagn, Mathias Nickl, Stefan Jörg, Georg Passig, Thomas Bahls, Alexander Nothhelfer, Franz Hacker, Luc Le-Tien, Alin Albu-Schäffer, Rainer Konietschke, et al. The dlr miro: a versatile lightweight robot for surgical applications. *Industrial Robot: An International Journal*, 35(4):324–336, 2008.

[37] Min Young Kim and Hyungsuck Cho. Technological trend of endoscopic robots. *Journal of Institute of Control, Robotics and Systems*, 20(3):345–355, 2014.

[38] Victoria J Fraser, Marilyn Jones, Patrick R Murray, Gerald Medoff, Yansheng Zhang, and Richard J Wallace Jr. Contamination of flexible fiberoptic bronchoscopes with mycobacterium che/onae linked to an automated bronchoscope disinfection machine1-3. *Am Rev Respir Dis*, 145:853–855, 1992.

[39] Alan H Ramsey, Tanya V Oemig, Jeffrey P Davis, Jeffrey P Massey, and Thomas J Toöroök. An outbreak of bronchoscopy-related mycobacterium tuberculosis infections due to lack of bronchoscope leak testing. *Chest*, 121(3):976–981, 2002.

[40] Cori L Ofstead, Mariah R Quick, Harry P Wetzler, John E Eiland, Otis L Heymann, David A Sonetti, and J Scott Ferguson. Effectiveness of reprocessing for flexible bronchoscopes and endobronchial ultrasound bronchoscopes. *Chest*, 154(5):1024–1034, 2018.

[41] Medhat S Hannallah, Jonathan L Benumof, and Urs E Ruttimann. The relationship between left mainstem bronchial diameter and patient size. *Journal of cardiothoracic and vascular anesthesia*, 9(2):119–121, 1995.

[42] Philippe Olivier, David Hayon-Sonsino, Jean Paul Convard, Pierre-Antoine Laloe, and Marc Fischler. Measurement of left mainstem bronchus using multiplane ct reconstructions and relationship between patient characteristics or tracheal diameters and left bronchial diameters. *Chest*, 130(1):101–107, 2006.

[43] Andriy Fedorov, Reinhard Beichel, Jayashree Kalpathy-Cramer, Julien Finet, Jean-Christophe Fillion-Robin, Sonia Pujol, Christian Bauer, Dominique Jennings, Fiona Fennessy, Milan Sonka, et al. 3d slicer as an image computing platform for the quantitative imaging network. *Magnetic resonance imaging*, 30(9):1323–1341, 2012.

[44] Philip J. Swaney. *Design and Modeling of Distal Dexterity Mechanisms For Needle-Sized Robots: Systems for Lung and Endonasal Interventions*. Ph.d. dissertation, Nashville, TN, 2016.

[45] Kyle B Reed, Ann Majewicz, Vinutha Kallem, Ron Alterovitz, Ken Goldberg, Noah J Cowan, and Allison M Okamura. Robot-assisted needle steering. *IEEE robotics & automation magazine*, 18(4):35–46, 2011.

[46] Ann Majewicz, Steven P Marra, Mark G van Vledder, MingDe Lin, Michael A Choti, Danny Y Song, and Allison M Okamura. Behavior of tip-steerable needles in ex vivo and in vivo tissue. *IEEE Transactions on Biomedical Engineering*, 59(10):2705–2715, 2012.

[47] Nick J van de Berg, Dennis J van Gerwen, Jenny Dankelman, and John J van den Dobbelsteen. Design choices in needle steeringa review. *IEEE/ASME Transactions on Mechatronics*, 20(5):2172–2183, 2015.

[48] Mark D O'Leary, Christina Simone, Toshikatsu Washio, Kiyoshi Yoshinaka, and Allison M Okamura. Robotic needle insertion: Effects of friction and needle geometry. In *Robotics and Automation, 2003. Proceedings. ICRA'03. IEEE International Conference on*, volume 2, pages 1774–1780. IEEE, 2003.

[49] Allison M Okamura, Christina Simone, and Mark D O'leary. Force modeling for needle insertion into soft tissue. *IEEE transactions on biomedical engineering*, 51(10):1707–1716, 2004.

[50] Sarthak Misra, Kyle B Reed, Benjamin W Schafer, KT Ramesh, and Allison M Okamura. Mechanics of flexible needles robotically steered through soft tissue. *The International journal of robotics research*, 29(13):1640–1660, 2010.

[51] Marta Scali, Tim P Pusch, Paul Breedveld, and Dimitra Dodou. Needle-like instruments for steering through solid organs: A review of the scientific and patent liter-

ature. *Proceedings of the Institution of Mechanical Engineers, Part H: Journal of Engineering in Medicine*, 231(3):250–265, 2017.

[52] Troy K Adebar, Joseph D Greer, Paul F Laeseke, Gloria L Hwang, and Allison M Okamura. Methods for improving the curvature of steerable needles in biological tissue. *IEEE Transactions on Biomedical Engineering*, 63(6):1167–1177, 2016.

[53] Robert J Webster, Jasenka Memisevic, and Allison M Okamura. Design considerations for robotic needle steering. In *Robotics and Automation, 2005. ICRA 2005. Proceedings of the 2005 IEEE International Conference on*, pages 3588–3594. IEEE, 2005.

[54] Thomas R Wedlick and Allison M Okamura. Characterization of pre-curved needles for steering in tissue. In *Engineering in Medicine and Biology Society, 2009. EMBC 2009. Annual International Conference of the IEEE*, pages 1200–1203. IEEE, 2009.

[55] Johnathan A Engh, Davneet S Minhas, Douglas Kondziolka, and Cameron N Riviere. Percutaneous intracerebral navigation by duty-cycled spinning of flexible bevel-tipped needles. *Neurosurgery*, 67(4):1117–1123, 2010.

[56] Ann Majewicz, Thomas R Wedlick, Kyle B Reed, and Allison M Okamura. Evaluation of robotic needle steering in ex vivo tissue. In *Robotics and Automation (ICRA), 2010 IEEE International Conference on*, pages 2068–2073. IEEE, 2010.

[57] Naresh V Datla, Bardia Konh, and Parsaoran Hutapea. A flexible active needle for steering in soft tissues. In *Bioengineering Conference (NEBEC), 2014 40th Annual Northeast*, pages 1–2. IEEE, 2014.

[58] Philip J Swaney, Peter A York, Hunter B Gilbert, Jessica Burgner-Kahrs, and Robert J Webster. Design, fabrication, and testing of a needle-sized wrist for surgical instruments. *Journal of medical devices*, 11(1):145011–145019, 2017.

[59] Johnathan A Engh, G Podnar, D Kondziolka, and Cameron N Riviere. Toward effective needle steering in brain tissue. In *Engineering in Medicine and Biology Society, 2006. EMBS'06. 28th Annual International Conference of the IEEE*, pages 559–562. IEEE, 2006.

[60] Jessica Burgner, Philip J Swaney, Ray A Lathrop, Kyle D Weaver, and Robert J Webster. Debulking from within: a robotic steerable cannula for intracerebral hemorrhage evacuation. *IEEE transactions on biomedical engineering*, 60(9):2567–2575, 2013.

[61] Richard J Hendrick, S Duke Herrell, and Robert J Webster. A multi-arm hand-held robotic system for transurethral laser prostate surgery. In *Robotics and Automation (ICRA), 2014 IEEE International Conference on*, pages 2850–2855. IEEE, 2014.

[62] Jessica Burgner, Philip J Swaney, Trevor L Bruns, Marlena S Clark, D Caleb Rucker, E Clif Burdette, and Robert J Webster. An autoclavable steerable cannula manual deployment device: Design and accuracy analysis. *Journal of medical devices*, 6(4):041007, 2012.

[63] Jessica Burgner, D Caleb Rucker, Hunter B Gilbert, Philip J Swaney, Paul T Russell, Kyle D Weaver, and Robert J Webster. A telerobotic system for transnasal surgery. *IEEE/ASME Transactions on Mechatronics*, 19(3):996–1006, 2014.

[64] Louise M Fanchon, Adytia Apte, C Ross Schmidtlein, Ellen Yorke, Yu-Chi Hu, Snjezana Dogan, Mathieu Hatt, Dimitris Visvikis, John L Humm, Stephen B Solomon, et al. Evaluation of the tumor registration error in biopsy procedures performed under real-time pet/ct guidance. *Medical physics*, 44(10):5089–5095, 2017.

[65] Sachin Patil, Jessica Burgner, Robert J Webster, and Ron Alterovitz. Needle steering in 3-d via rapid replanning. *IEEE Transactions on Robotics*, 30(4):853–864, 2014.

[66] Thomas Cooper and Craig R Ramstad. Sterile drape interface for robotic surgical instrument, February 15 2011. US Patent 7,886,743.

[67] Hunter B Gilbert, D Caleb Rucker, and Robert J Webster III. Concentric tube robots: The state of the art and future directions. In *Robotics Research*, pages 253–269. Springer, 2016.

[68] John P Swensen, MingDe Lin, Allison M Okamura, and Noah J Cowan. Torsional dynamics of steerable needles: modeling and fluoroscopic guidance. *IEEE Transactions on Biomedical Engineering*, 61(11):2707–2717, 2014.

[69] Vinutha Kallem and Noah J Cowan. Image guidance of flexible tip-steerable needles. *IEEE Transactions on Robotics*, 25(1):191–196, 2009.

APPENDIX

Manufacturing Flexure-Tip Needles

The flexure-hinge needle tip is made through a CNC-manufacturing process detailed in [44] used to make the needle-sized wrist. The flexure-hinge, and cutting the needle tip segment to length, are made by milling a cross sectional slot through the wall of the tube.

1. We have found success creating the bevel tip by using a grinding wheel to file the needle tip tube to an angled surface on a fixture block. The angled fixture block is made by drilling a hole in the side of the block, which is positioned using angled parallels of the desired bevel angle. We created a single fixture to make bevel angles of 5,10,15,20,25,30°increments in testing shown in Figure 2 (*A*).

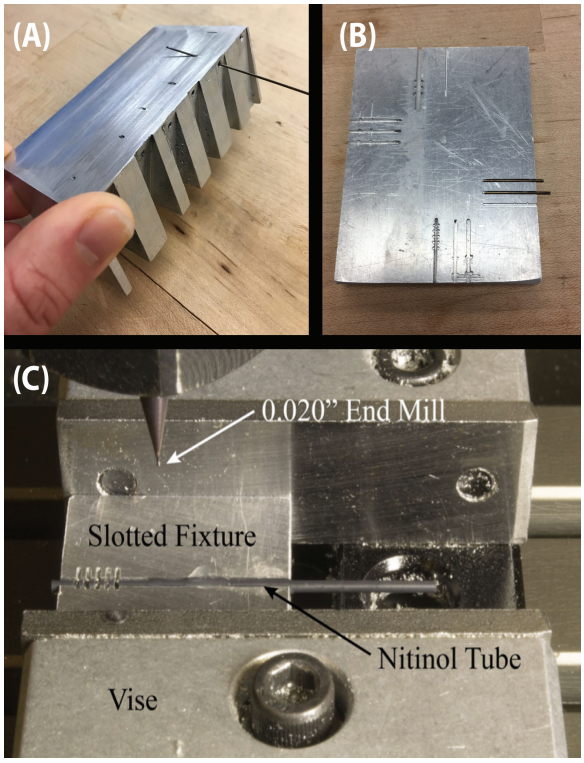

Figure 2: (*A*) block used for grinding the bevel angle (*B*) needle tips placed bevel side down into the fixture (*C*) CNC set up for machining the slots into the needle

2. After the needle tip is ground to the appropriate bevel, we glue the needle into a fixture of approximately the same slot diameter as the needle tip. The beveled surface

lies directly into the fixture as shown in Figure 2 (*B*), to result in a flexure-hinge on the opposite side of the bevel.

3. The flexure hinge slot and the cut-off of the needle tip are then manufactured using an end mill corresponding to the desired cut-width parameter. Figure 2 (*C*) shows the CNC set up used in both the manufacturing of the needle and the wrist.

4. To release the tip out of the fixture, soak it in acetone for 20 minutes, or we have had success removing the adhesive bind with a hot air gun

5. Integrating the sensor into the needle requires feeding the coils through the length of the shaft before soldering the connector for the NDI system. We've had success feeding the sensor wires down the shaft by means of a long guide wire that pulls the sensor wires through the needle shaft. Place a drop of Loctite 401 on the sensor wire ends to the guide wire, and feed it through the shaft.

6. With the sensor coil at the tip of the needle shaft, guide the machined flexure-hinge needle tip over the sensor and fit onto the shaft, adhering it with JBWeld Epoxy.